Clinopyroxene/Melt Trace Element Partitioning in Sodic Alkaline Magmas

Charles D. Beard [1,2]*, Vincent J. van Hinsberg[2], John Stix[2] and Max Wilke[3,4]

[1]British Geological Survey, The Lyell Centre, Research Avenue South, Edinburgh EH14 4AP, UK; [2]Department of Earth and Planetary Sciences, McGill University, 3450 University Street, Montreal, Québec H3A 0E8, Canada; [3]Institut für Geowissenschaften, Universität Potsdam, Golm, Germany; [4]Chemie und Physik der Geomaterialien, Deutsches GeoForschungsZentrum GFZ, Potsdam, Germany

*Corresponding author. Telephone: +44 (0)131 650 0336. E-mail: charles.beard@mail.mcgill.ca

Received March 4, 2019; Accepted November 7, 2019

ABSTRACT

Clinopyroxene is a key fractionating phase in alkaline magmatic systems, but its impact on metal enrichment processes, and the formation of REE + HFSE mineralisation in particular, is not well understood. To constrain the control of clinopyroxene on REE + HFSE behaviour in sodic (per)alkaline magmas, a series of internally heated pressure vessel experiments was performed to determine clinopyroxene–melt element partitioning systematics. Synthetic tephriphonolite to phonolite compositions were run H_2O-saturated at 200 MPa, 650–825°C with oxygen fugacity buffered to log $fO_2 \approx \Delta FMQ + 1$ or log $fO_2 \approx \Delta FMQ +5$. Clinopyroxene–glass pairs from basanitic to phonolitic fall deposits from Tenerife, Canary Islands, were also measured to complement our experimentally-derived data set. The REE partition coefficients are 0·3–53, typically 2–6, with minima for high-aegirine clinopyroxene. Diopside-rich clinopyroxene ($Aeg_{5–25}$) prefer the MREE and have high REE partition coefficients (D_{Eu} up to 53, D_{Sm} up to 47). As clinopyroxene becomes more Na- and less Ca-rich ($Aeg_{25–50}$), REE incorporation becomes less favourable, and both the $^{VI}M1$ and $^{VIII}M2$ sites expand (to 0·79 Å and 1·12 Å), increasing D_{LREE}/D_{MREE}. Above Aeg_{50} both M sites shrink slightly and HREE ($^{VI}r_i \leq 0.9$ Å $\approx$ Y) partition strongly onto the $^{VI}M1$ site, consistent with a reduced charge penalty for $REE^{3+} \leftrightarrow Fe^{3+}$ substitution. Our data, complemented with an extensive literature database, constrain an empirical model that predicts trace element partition coefficients between clinopyroxene and silicate melt using only mineral major element compositions, temperature and pressure as input. The model is calibrated for use over a wide compositional range and can be used to interrogate clinopyroxene from a variety of natural systems to determine the trace element concentrations in their source melts, or to forward model the trace element evolution of tholeiitic mafic to evolved peralkaline magmatic systems.

Key words: aegirine; experimental petrology; Canary Islands; peralkaline; rare earth elements

INTRODUCTION

Trace element systematics provide a powerful methodology to investigate and model magmatic processes (Spera & Bohrson, 2001; Troll & Schmincke, 2002; Boudreau, 2004; Xu *et al.*, 2010; Girnis *et al.*, 2013; Mungall & Brenan, 2014), but their interpretation requires precise knowledge of mineral/liquid element partition coefficients. The approach has been applied to studies of mafic systems and mantle melting processes (Niu, 2004; Workman & Hart, 2005; Foley *et al.*, 2013; Coumans *et al.*, 2016; Peters *et al.*, 2017). However, poor constraints on element partitioning behaviour in alkaline and peralkaline rocks thus far preclude widespread application in these systems.

Sodic clinopyroxene appear to more readily incorporate REE than their calcic equivalents (Marks *et al.*, 2004), but despite fractionation of these minerals, melts in evolved (per)alkaline systems can attain high REE contents, even up to economic levels (Typically considered ~1 wt % total Rare Earth Oxides; Kogarko, 1990; Downes *et al.*, 2005; Marks *et al.*, 2011; Sjöqvist *et al.*, 2013; Goodenough *et al.*, 2016; Möller & Williams-Jones, 2016; Borst *et al.*, 2018). Precise knowledge of mineral/liquid partition coefficients for REE is required to forward model the effects of crystal fractionation on metal enrichment in residual liquids, and thus to understand the magmatic portion of the REE enrichment history of these systems. Furthermore, this facilitates interrogation of clinopyroxene from successive units of REE-mineralised nepheline syenite systems (cf. van Hinsberg *et al.*, 2010; Slack & Trumbull, 2011; Dare *et al.*, 2014; Vasyukova & Williams-Jones, 2019) and may reveal metal enrichment paths in ephemeral melts, providing insight into the relative importance of magmatic and hydrothermal processes for mineralisation.

Experimental investigations of element partitioning behaviour in alkali-enriched systems are limited in terms of composition (Wood & Trigila, 2001; Huang *et al.*, 2006), and none yet have explored peralkaline conditions where molar (Na+K)/Al exceeds 1. Additional information has been obtained from natural samples by measuring the concentration ratios of phenocryst–glass pairs from volcanic and intrusive rocks (Larsen, 1979; Wörner *et al.*, 1983; Shearer & Larsen, 1994; Fedele *et al.*, 2009; Severs *et al.*, 2009; Mollo *et al.*, 2016). However, these results may be biased by the presence of melt inclusions, mineral inclusions and mineral zoning, and their interpretation is commonly complicated by unknown or poorly constrained P–T–H_2O–fO_2 conditions of equilibration and assumptions of closed-system behaviour.

In this contribution, we present trace element partition coefficients between sodic clinopyroxene and silicate melts of tephriphonolite to phonolite composition, as determined from internally heated pressure vessel experiments on synthetic and natural compositions. These are complemented by well-constrained natural volcanic phenocryst-glass pairs from Canary Islands pyroclastic fall deposits. We characterise the mineral compositional controls on element partitioning behaviour and present a predictive model for clinopyroxene/melt element partitioning that can be used to generate clinopyroxene/melt partition coefficients using only clinopyroxene major element compositions (e.g. as measured by electron-microprobe). This approach permits forward modelling of element budgets during differentiation processes in magmatic systems, including evolved sodic alkaline systems, as well as providing a mineral-based tool that can be used to reconstruct parental melt compositions from clinopyroxene compositions in natural rocks.

METHODOLOGY

Experimental starting materials

Clinopyroxene was synthesised in sodic alkaline silicate melts of varying composition to obtain a range of mineral compositions consistent with those in natural systems. Starting glass compositions are given in Table 1 and Supplementary Data Figs S1 and S2; supplementary data are available for downloading at http://www.petrology.oxfordjournals.org. Synthetic glasses L1 and L5 were prepared from reagent-grade oxide and carbonate powders, ground together in an agate mortar, decarbonated for 6 hrs at 450°C, and then homogenised in air for 3 hrs at 1400°C in a Pt crucible. Repeated fusion and grinding in agate ensured chemical homogeneity of the starting glasses, which was confirmed by electron microprobe analyses of the final fused glass. Finely ground Mud Tank zircon was added to the homogeneous major element glasses as a source of Zr, Hf, Nb and Ta; the glasses were then fused for a further three hours at 1400°C. The remaining trace elements were added as a cocktail of single element nitrate solutions (ICP-MS standards), dried onto the powdered glasses and then denitrified at 450°C for 30 minutes. The synthetic basanite L1 and phonolite L5 were mixed in varying proportions to make the low alkali (L) series of starting glasses, while dried NaOH and KOH powders were added to make the middle (M) and high (H) alkali starting glasses. Analyses of glass compositions L5 and H5, quenched from super-liquidus conditions, confirm that the melt was homogeneous at the start of the experiments (Supplementary Data Electronic Appendix 1).

A well-mixed rock powder from the Nechalacho Layered Suite in Canada (Möller & Williams-Jones, 2016, Unit NLS-9, sample L09-194–405·5, alternative sample name *VM 11–6*) was used as experimental starting material for a more extreme peralkaline composition. This composition was not fused prior to loading into experiment capsules, so as to preserve the original volatile element concentrations. An experiment using this material that was quenched from super-liquidus conditions is homogeneous with respect to major elements, as determined from electron microprobe measurements.

Experimental equipment and procedures

In total, 36 partitioning experiments were conducted in a Harwood-type internally heated pressure vessel (IHPV) in the HP-GeoMatS laboratory at the Deutches GeoForschungsZentrum in Potsdam, Germany (Supplementary Data Electronic Appendix 1). Temperature was measured with Type-S thermocouples calibrated against the melting point of NaCl (Borchert *et al.*, 2010, accuracy of ± 5 °C at 200 MPa) at the top, middle and bottom of the furnace and showed there to be no thermal gradient over the capsule. Argon gas was used as the pressure medium, and pressure was measured with a strain gauge to an accuracy of ± 7 MPa. During the

Table 1: Major-element oxide compositions of starting materials for the internally heated pressure vessel experiments

Dry starting glass compositions calculated from masses of reagents added [wt %]										[mol]
Composition	SiO$_2$	TiO$_2$	Al$_2$O$_3$	FeO(T)	MgO	CaO	Na$_2$O	K$_2$O	Total	(Na+K)/Al
L4	57·48	1·50	19·00	5·89	1·61	3·21	7·33	3·98	100	0·861
L5	61·24	0·68	19·51	3·77	0·43	0·91	8·63	4·84	100	0·996
M3	52·67	2·27	18·13	7·86	2·75	5·40	7·19	3·73	100	0·875
M4	56·35	1·47	18·63	5·77	1·58	3·15	8·48	4·57	100	1·014
M5	60·04	0·66	19·13	3·69	0·42	0·89	9·76	5·41	100	1·145
H4	54·80	1·43	18·12	5·62	1·54	3·06	10·07	5·38	100	1·236
H5	58·38	0·65	18·60	3·59	0·41	0·86	11·31	6·20	100	1·362
Water saturated glass compositions from superliquidus experiments (EPMA) [wt%]										[mol]
L5	57·46	0·643	16·59	2·363	0·404	0·985	7·84	4·462	90·75	1·069
s.d. (n = 8)	0·299	0·087	0·210	0·059	0·035	0·050	0·175	0·132	0·351	0·017
rsd	0·52%	13·58%	1·26%	2·51%	8·70%	5·09%	2·23%	2·97%	0·39%	1·57%
H5	55·58	0·612	16·21	2·568	0·422	0·906	10·77	5·732	92·8	1·476
s.d. (n = 13)	0·327	0·057	0·221	0·113	0·044	0·049	0·205	0·154	0·417	0·028
rsd	0·59%	9·33%	1·36%	4·41%	10·44%	5·40%	1·90%	2·69%	0·45%	1·87%
Mineralized natural system composition (ICP-AES)* [wt %]										[mol]
NLS-9	55·60	0·02	17·40	9·54	0·01	1·16	11·90	2·26	99·30	1·266

*Nechalacho layered suite, NT, Canada; analyses from Möller & Williams-Jones (2016).

experiments, pressure was controlled automatically and held within ± 50 MPa of stated values.

Oxygen fugacity was buffered to the intrinsic redox conditions of the experimental setup, which corresponds to log fO_2 *ca* ΔFMQ +1 in our H$_2$O saturated charges (see Chou, 1986; Berndt *et al.*, 2002; Jugo *et al.*, 2010, FMQ is the fayelite-magnetite-quartz oxygen buffer). One experiment using the Nechalacho Layered Suite composition was performed in a double capsule with a haematite solid buffer, designed to increase fO_2 and promote crystallization of Fe^{3+}-rich clinopyroxene (Eugster & Wones, 1962). This experiment ran at the Hm-Mt buffer, which corresponds to log $fO_2 \approx$ ΔFMQ +5, as confirmed by presence of both buffer minerals in the outer capsule following quench. Experimental temperatures were chosen to produce run products with a high proportion of melt relative to crystals for each of the compositions, and were found by trial and error to be 650 to 825°C, all at 200 MPa pressure (Table 2 and Supplementary Data Electronic Appendix 1).

Powdered starting glass and distilled, deionised water were welded inside 3·0 or 3·5 mm outer diameter platinum capsules of 20–25 mm length (see Supplementary Data Electronic Appendix 1). To verify that capsules were sealed, they were heated to 110°C and weighed before and after, as well as at the end of the run. The amount of water sealed inside the capsules varied with temperature and composition and was kept in excess of saturation (Carroll & Blank, 1997; Moore *et al.*, 1998; Schmidt & Behrens, 2008). Water saturation was confirmed post-run by puncturing capsules and checking for water expulsion and mass loss on drying at 110°C.

The capsules were loaded into the vessel, pressurised to 200 MPa, then heated to super-liquidus temperatures for at least 16 hrs (Supplementary Data Electronic Appendix 1) to permit homogenisation of trace element concentrations, dissolution of water, and equilibration of fO_2 by exchange of H$_2$ through the capsule wall (Gaillard *et al.*, 2002). Following homogenisation, temperature was lowered to run conditions. An initial set of experiments were cooled rapidly from homogenisation to run temperature at about 100°C/min. A second set of experiments were cooled to run temperature at 1°C/min to promote slow growth of crystals and to minimise the formation of compositional gradients in the melt. Vessel temperature was then cycled twice between run temperature (held for 30 min) and run temperature + 10°C (held for 30 min, followed by cooling at 1°C/min) to promote dissolution of small crystals at the expense of larger grains, and to promote crystal growth close to the run temperature. Element partitioning results are consistent among experiments of different cooling paths. In all experiments, run temperature was maintained for >40 hrs to allow for chemical homogenisation of melt and growth of crystals via Ostwald ripening. Capsules were then quenched to room temperature.

To minimise the growth of groundmass crystals on cooling, a rapid-quench apparatus was used where possible (Table 2). We have not measured quench rates in this vessel, but the capsules probably cooled at rates of several hundred degrees Celsius per second (e.g. Berndt *et al.*, 2002). For the rest of the experiments, quenching was achieved by cutting power to the furnace, which resulted in cooling to below the glass-transition temperature (<350°C; Giordano *et al.*, 2005) in less than 150 seconds.

Natural samples

Experiments are complemented with natural samples of clinopyroxene-bearing phonolite and basaltic trachyandesite from Tenerife, Canary Islands. Alkaline volcanism on Tenerife is associated with a weak thermal mantle plume that impinges upon thick, old, slow-

Table 2: Summary of run conditions and run products for the internally-heated pressure vessel experiments

Charge	Setup	Pressure	Cooling ramp		TE-1/ TE-3	TE-2 (spls)	Time (after ramp)	Run products
			Rate °C/min	Cycle +10°C				
		[MPa]			[°C]	[°C]	[hr]	
L4$_3$	IHPV_RQ (f)	203·8	1	Y	825	828	44h50m	Cpx + Ox + Ttn + Melt + Vap
L5$_3$	IHPV_RQ (f)	203·8	1	Y	825	828	44h50m	Cpx + Ox + Melt + Vap
M3$_2$	IHPV_RQ	202·0	1	Y	796/795	799	47hr	Cpx + Ox + Bt + Melt + Vap
M4$_4$	IHPV_RQ	202·0	1	Y	796/795	799	47hr	Cpx + Ox + Bt + Melt + Vap
M5	IHPV	200·0	–	–	800	799	47h55m	Cpx + Bt + Fsp + Melt + Vap
M5$_2$	IHPV_RQ	200·0	–	–	700	689	45h45m	Cpx + Bt + Fsp + Melt + Vap
H4$_2$	IHPV	200·0	–	–	800	799	47h55m	Cpx + Ttn + Melt + Vap
H5$_2$	IHPV_RQ	200·0	–	–	700	689	45h45m	Cpx + Bt + Fsp + Melt + Vap
H5$_3$	IHPV_RQ	202·0	–	–	651/649	648	46h15m	Cpx + Bt + Fsp + Melt + Vap
NLS-9	IHPV_RQ	202·0	1	Y	651/649	648	46h15m	Cpx + Ox + Melt + Vap
NLS-9$_2$HM	IHPV_RQ**	200·0	1	Y	650	655	42hr	Cpx + Ox + Fsp + Melt + Vap

_RQ indicates use of a rapid-quench apparatus; (f) indicates failure of the rapid-quench apparatus, where capsules became jammed in the hot-zone of the IHPV (i.e. equiv. to regular quench); ** indicates use of a haematite double capsule, for run conditions at the haematite–magnetite fO_2 buffer (Eugster and Wones, 1962). TE-1 and TE-3 indicate run temperatures as measured by Type-S thermocouples at the top and bottom of the experimental capsules, respectively. TE-2 indicates run temperature measured level with the centre of the experimental capsules. Cpx, clinopyroxene; Ox, spinel oxide; Ttn, titanite; Bt, biotite; Fsp, sanidine feldspar; Vap, aqueous vapour.

moving oceanic lithosphere (Carracedo *et al.*, 2007). This geological scenario has favoured development of a complex magma-plumbing system that produces a great diversity of volcanic products from alkali basalt to phonolite in composition (Wiesmaier *et al.*, 2012). The Las Cañadas edifice, a large, central, composite stratovolcano (Bryan *et al.*, 1998; Brown *et al.*, 2003; Edgar *et al.*, 2007), rests upon a base of at least three mafic alkaline shield volcanoes (Thirlwall *et al.*, 2000; Guillou *et al.*, 2004; Gurenko *et al.*, 2006) Xenoliths indicate that a nepheline syenite intrusive system underlies the island (Wiesmaier *et al.*, 2012).

Six clinopyroxene/glass pairs from four separate volcanic eruptions on Tenerife were selected because they are free from alteration, the clinopyroxene showed no concentric or sector zoning in BSE images and the adhered glass was of suitable size for *in situ* chemical analyses (e.g. Fig. 1). The studied eruptive units are the $\sim$ 2 ka phonolitic plinian fall deposits from Montaña Blanca and Pico Viejo (Ablay *et al.*, 1995), which represent the only known substantial post-caldera explosive activity on Tenerife. Phase equilibrium experiments conducted on Montaña Blanca unit UMB-II suggest that magma was stored prior to eruption at 850 ± 15°C, 50 ± 20 MPa, with 2·5 ± 0·5 wt % H_2O at log $fO_2 \approx$ NNO - 0·5 (Andújar & Scaillet, 2012). We also measured a cpx-glass pair from Montaña Samara, a monogenetic mafic cinder cone situated $\sim$ 2 km NW of the Las Cañadas caldera rim (Albert *et al.*, 2015). Field locations, mineral proportions and major element compositions of the clinopyroxene and glasses are presented in Supplementary Data Electronic Appendix 1 and 2.

Sample preparation

Experiment capsules were torn open with pliers, and charges were split using a low-speed wafering saw.

Samples were mounted in epoxy resin and polished for *in situ* chemical analysis.

Natural pyroclastic rocks were rinsed in tap water and crushed with a hammer. Crystals with adhered glass, hand-picked from a sieved size fraction between 125 μm and 1·18 mm, were used to make grain mounts containing 5–20 crystals of clinopyroxene per sample. Natural samples also contain biotite, sanidine, ± spinel, amphibole, olivine, titanite and sodalite. Clinopyroxene mineral mounts were examined using backscattered electron imaging to select euhedral crystals that were free from melt inclusions and chemical zoning (n = 6, Fig. 1).

ANALYTICAL TECHNIQUES

All experimental products were examined by reflected light optical microscopy and scanning electron microscopy, and all phases produced were identified by electron microprobe using an energy-dispersive spectrometer. Backscatter electron images were obtained to estimate modal proportions of phases, which were calculated using ImageJ freeware (Rasband, 2016; see Supplementary Data Electronic Appendix 1).

Electron microprobe analysis

Major element compositions of experimental products and natural minerals and glasses were measured with a JEOL 8900 EPMA instrument at McGill University and a JEOL 8230 EPMA instrument at the University of Ottawa, both using wavelength dispersive spectrometers (Table 3). An accelerating voltage of 15 kV was used with a 15 nA beam of 5 μm diameter for minerals, and a 4 nA beam of 50 μm diameter for glasses. Count times for all elements were 60 sec. Using the above routine,
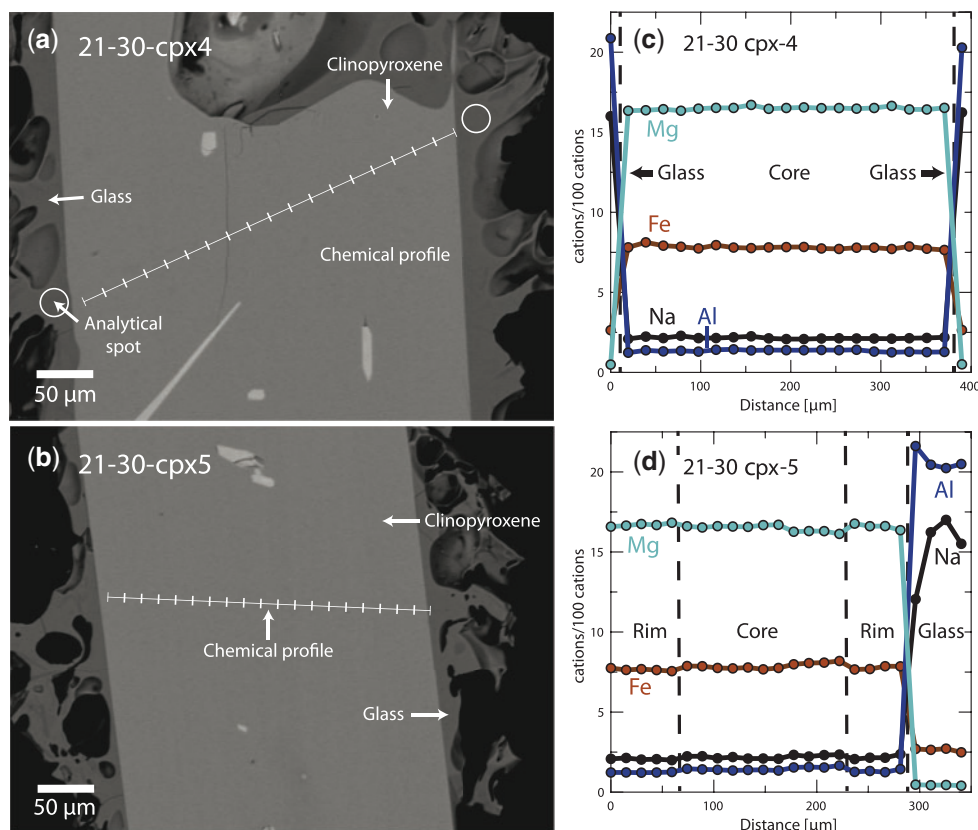
Fig. 1. Examples of textural features from Canary Islands clinopyroxene phenocrysts from this study and corresponding diagrams showing chemical profiles. (a, b) Backscattered electron images show that crystals are euhedral and are free from complex zoning patterns. (c, d) Diagrams of Mg, Fe, Al and Na profiles of across clinopyroxene phenocrysts and glass rims (quenched melt), as measured by EPMA-WDS, show that zoning is effectively absent in this clinopyroxene. Glass analyses shown in (d) are from rims of quenched melt from other clinopyroxene phenocrysts recovered from the same pumice sample. Both pictured phenocrysts are from the basal air fall deposit associated with the ~2 ka plinian eruption of Pico Viejo, Tenerife (Ablay *et al.*, 1995).

we observed no sodium loss over the measurement time period. For the silicate minerals and glasses, both synthetic and natural minerals or oxides were used for calibration (see Supplementary Data Electronic Appendix 1). Analytical uncertainties were determined by multiple analyses of reference materials and duplicate analyses of samples.

Element distribution maps were generated with a JEOL 8900 instrument at McGill University using an accelerating voltage of 15 kV, a focussed 40 nA beam, and a dwell time of 50 ms per pixel (Fig. 3 and Supplementary Data Fig. S3). Fe, Ti, Al, Si and Na were measured with wavelength-dispersive detectors, while Ca and Mg were measured with an energy-dispersive spectrometer.

Transects of Ce, Mg and Fe concentrations across the experimental clinopyroxene were measured with a JEOL 8900 instrument at McGill University using a focussed beam of 50 nA with an accelerating voltage of 20 kV. Ce was counted with a wavelength-dispersive spectrometer with an LIFH crystal for 100 sec (MAC-Ce standard). Mg and Fe were counted for 20 sec, with TAP and LIF crystals respectively (diopside and olivine standards, respectively).

Laser-ablation ICP-MS

Trace element concentrations in clinopyroxene and glass were determined by laser-ablation ICP-MS. Analyses were performed at McGill University using a NewWave 213 nm Nd-YAG laser system coupled to a Thermo Finnigan iCAP-Qc quadrupole ICP-MS instrument. Typical fluence was 3–12 J/cm^2 (from 80 μm to 8 μm spot sizes), with a repetition rate of 10 Hz. Ablated material was transferred to the ICP-MS in a He flow of 800 mL/min and mixed with Ar prior to injection into the plasma. Instrumental drift was monitored by repeat analyses of the primary standard glass BCR-2G, with bias monitored by repeat analyses of secondary standards UTR-2 peralkaline rhyolite and USGS-RGM-1 rhyolite glasses (Supplementary Data Electronic Appendix 1). Sample surfaces were pre-ablated to remove residues from polishing materials and to improve ablation efficiency.

Primary and secondary standard glasses and an unzoned Canary Islands clinopyroxene were analysed with beam sizes of 8–80 μm to check for crater size-dependent element fractionation effects; none were found for the elements reported here. For minerals and glasses in the experimental charges, beam sizes of

Table 3: Representative major-element oxide compositions of clinopyroxene and melt for the internally heated pressure vessel experiments and Canary Islands phenocryst–glass pairs

Clino-pyroxene	IHPV experiments						16-07 px4 LMB	17-12 pxs-4 Samara	17-14 pxs-1 UMB-II	21-30 px-4 PV 2 Ka
	$L4_3$	$M3_2$	$M5_2$	$H5_3$	NLS-9	$NLS-9_2HM$				
SiO_2	44·70	40·73	47·31	46·95	50·73	51·90	52·43	51·77	51·81	52·50
TiO_2	3·07	4·57	3·17	4·47	0·10	0·10	0·80	0·78	0·74	0·75
Al_2O_3	5·23	9·26	3·08	3·10	2·46	2·96	1·33	1·24	1·27	1·22
FeO	13·31	11·72	18·84	16·95	28·14	28·61	9·71	9·62	10·51	10·02
MnO	0·01	0·01	0·01	0·00	0·25	0·17	0·78	0·84	0·91	0·81
MgO	9·09	9·28	5·55	6·05	0·05	0·07	12·30	12·64	12·07	11·88
CaO	19·49	22·17	16·11	15·29	5·88	3·14	21·90	21·76	21·52	22·02
Na_2O	2·27	1·01	4·34	4·97	9·86	11·45	1·18	1·17	1·38	1·19
K_2O	0·09	0·03	0·08	0·07	0·04	0·04	0·02	0·03	0·00	0·02
Total	97·25	98·78	98·49	97·85	97·49	98·45	100·44	99·85	100·22	100·42
Glass										
SiO_2	58·79	57·29	57·45	54·91	58·17	58·14	60·38	55·10	59·08	60·04
TiO_2	0·35	0·27	0·23	0·62	0·00	0·00	0·64	1·73	0·66	0·66
Al_2O_3	17·35	19·14	16·69	16·06	18·55	19·41	19·96	18·30	19·68	19·79
$Fe_2O_3(T)$	2·35	1·35	1·01	3·16	1·67	1·91	3·65	7·22	4·02	3·96
FeO(T)	2·12	1·22	0·91	2·84	1·50	1·72	3·28	6·49	3·62	3·56
MnO	0·02	0·00	–	0·01	0·06	0·04	0·14	0·23	0·22	0·20
MgO	0·20	0·13	0·15	0·35	0·00	0·00	0·39	1·84	0·32	0·35
CaO	0·55	0·95	0·24	0·84	0·23	0·23	0·76	4·10	0·77	0·74
Na_2O	7·17	7·32	9·08	8·88	11·12	9·80	9·00	7·26	9·76	9·05
K_2O	4·68	4·10	4·68	5·30	1·51	2·51	5·41	4·09	5·45	5·57
Total	91·23	90·41	89·43	89·81	91·15	91·85	99·95	99·13	99·56	99·95
(Na+K)/Al	0·97	0·86	1·15	1·27	1·07	0·97	1·01	1·12	1·09	1·09

All values in wt %, except (Na + K)/Al, which is a unitless molar ratio. LMB, the lower Montaña Blanca unit; UMB-II, the upper Montaña Blanca unit II; PV 2 Ka, the c.2 kyr basal pyroclastic fall deposit of Pico Viejo, all phonolites from Tenerife (Ablay et al., 1995). Montaña Samara is a monogenetic mafic cinder cone, also on Tenerife (Albert et al., 2015).

8–40 μm and 16–80 μm were used, respectively. Depending on grain size and availability, 5–14 mineral grains and 3–10 areas of glass were analysed per charge. Natural clinopyroxene and rim glasses were analysed using a beam size of 12–80 μm and 12–30 μm, respectively. Wherever possible, mineral cores were avoided and ablation was performed along lines parallel to crystal rims (1–3 μm /sec).

Drift corrections and data reduction were conducted with the iolite v2.5 extension for Igor Pro (Paton et al., 2011). The total of major elements measured by LA-ICP-MS or, where available, the Al concentration from electron microprobe analyses, was used as an internal standard (Supplementary Data Electronic Appendix 1). For some experiments, ablation through the minerals was too rapid to generate a stable signal for data reduction purposes. In these cases, a mixing model was applied to estimate the composition of this clinopyroxene following Yang et al. (2018); see Supplementary Data Electronic Appendix 3. Trace element partition coefficients derived from these two data reduction methodologies are consistent to better than 2σ.

RESULTS

Run product phase stability and crystallinity
Trace element data are reported for eleven experimental charges. 25 additional experiments were rejected as their run temperatures were super-liquidus or sub-solidus, or because their growth textures were indicative of disequilibrium (e.g. Supplementary Data Fig. S3).

Phase proportions are given in Supplementary Data Electronic Appendix 1.

All reported experimental runs were near-liquidus (3–22% crystals) and are characterised by a homogeneous distribution of phases (Fig. 2 and Supplementary Data Fig. S3), except for experiments $H5_3$ and NLS-9_2_HM, in which sanidine crystals are concentrated at the centre. Glasses are clean, homogeneous and show a limited range of major and trace element compositions for each experiment (Supplementary Data Fig. S1 and S2). Clinopyroxene crystals are generally small, euhedral blades with a narrow range of sizes for a given experiment (<10 μm to 100 μm minor axis in cross section, Figs 2 and 3). In addition to clinopyroxene and glass, experiments on mafic to intermediate compositions produced magnetite, titanite ± kaersutite amphibole, whereas some phonolitic experiments produced biotite, alkali feldspar ± magnetite (Supplementary Data Electronic Appendix 1).

Constraining the full phase equilibria of all of the investigated compositions was beyond the scope of this study. However, in our experiments it can be seen that clinopyroxene has a wide stability field across the investigated physico-chemical conditions with only a single starting composition generating amphibole in place of pyroxene (experiments L3 and $L3_2$). Run conditions and run products given in Table 2.

Glass compositions
All run-product glasses are homogeneous across the length and width of the experimental capsules based on
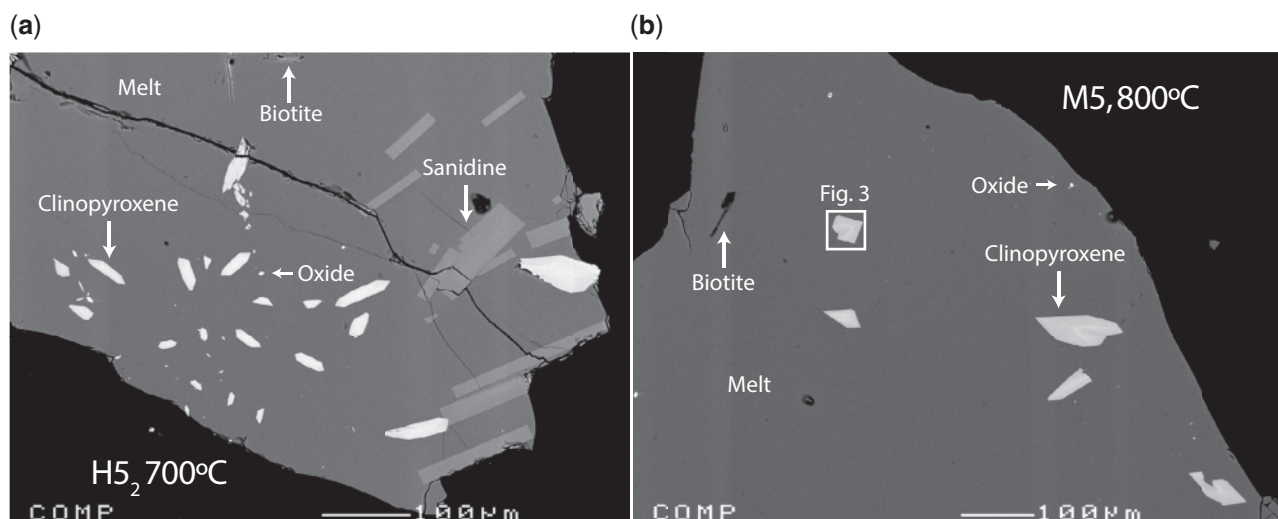
Fig. 2. Backscattered electron images of typical run products from the internally heated pressure vessel experiments. Crystal fractions are typically small (<10% by area), with blade-shaped, euhedral clinopyroxene and glasses free of quench crystals.
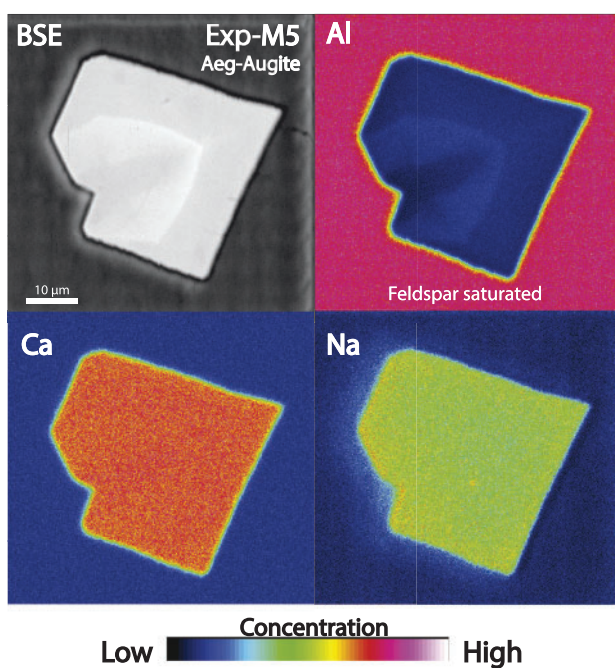

Fig. 3. EPMA-WDS element maps of clinopyroxene from internally heated pressure vessel experiment M5 (see box in Fig. 2b for position). Aegirine–augite clinopyroxene has a sharp internal boundary in Al that reflects feldspar saturation. Further element maps are given in Supplementary Data Fig. S3.

multiple electron microprobe and laser ablation ICP-MS analyses. The major element oxide compositions, as measured by electron microprobe, show relative standard deviations of <5% within experiment capsules, with minor element oxides (concentration <1%) showing greater variability, most with standard deviations between 5 and 10% relative (see Supplementary Data Electronic Appendix 1). Trace element compositions of the glass, as measured by laser-ablation ICP-MS, typically show time-weighted relative standard deviations of

1 to 8% within each capsule, with this variability depending on both the absolute concentration of that element and on the beam-size that was used for the analyses (Supplementary Data Electronic Appendix 1). Low totals of major element oxide concentrations in the electron microprobe analyses are a result of high dissolved water contents in the quenched melt.

On a total-alkalis vs silica diagram the experiment glasses are predominantly phonolitic in composition, though span the trachyte–phonolite join (Supplementary Data Fig. S1). Their alkalinity index (molar (Na + K)/Al) is 0·85 to 1·40, crossing the alkaline–peralkaline join, and the Mg# of these quenched melts is 0 (Mg-free) to 22. The dissolved water content of these quenched melts is 8·8 to 10·7 wt % (by difference method from EPMA data, with the Fe oxidation state assigned following Kress & Carmichael, 1991) and their NBO/T ratios are 0·98 to 1·42 (Mysen *et al.*, 1982, 1985; the ratio of non-bonding oxygen anions to tetrahedral cations in the melt). The halogen content of the synthetic experiments is nominally zero, whereas glasses from the Nechalacho Layered Suite composition experiments typically contain 0·1% F and 0·02% Cl by weight.

The Canary Islands glasses are mostly trachytic to phonolitic, with one basaltic trachyandesite (sample 17–12, Montaña Samara), and are alkaline to weakly peralkaline in composition (A.I. of 0·78 to 1·16) with Mg# of 8 to 39. Dissolved water content and NBO/T ratios are not reported for these glasses because of post-eruptive loss of volatiles. These Canary Islands glasses typically contain 0·2% F and 0·4% Cl by weight.

Compositions of the clinopyroxene and major element exchange

Experiments on the synthetic compositions produced clinopyroxene of diopside to aegirine–augite composition (Di_{29-82}, Aeg_{9-45} Hd_{7-33}), a subset of which overlap with the compositional space defined by the Canary
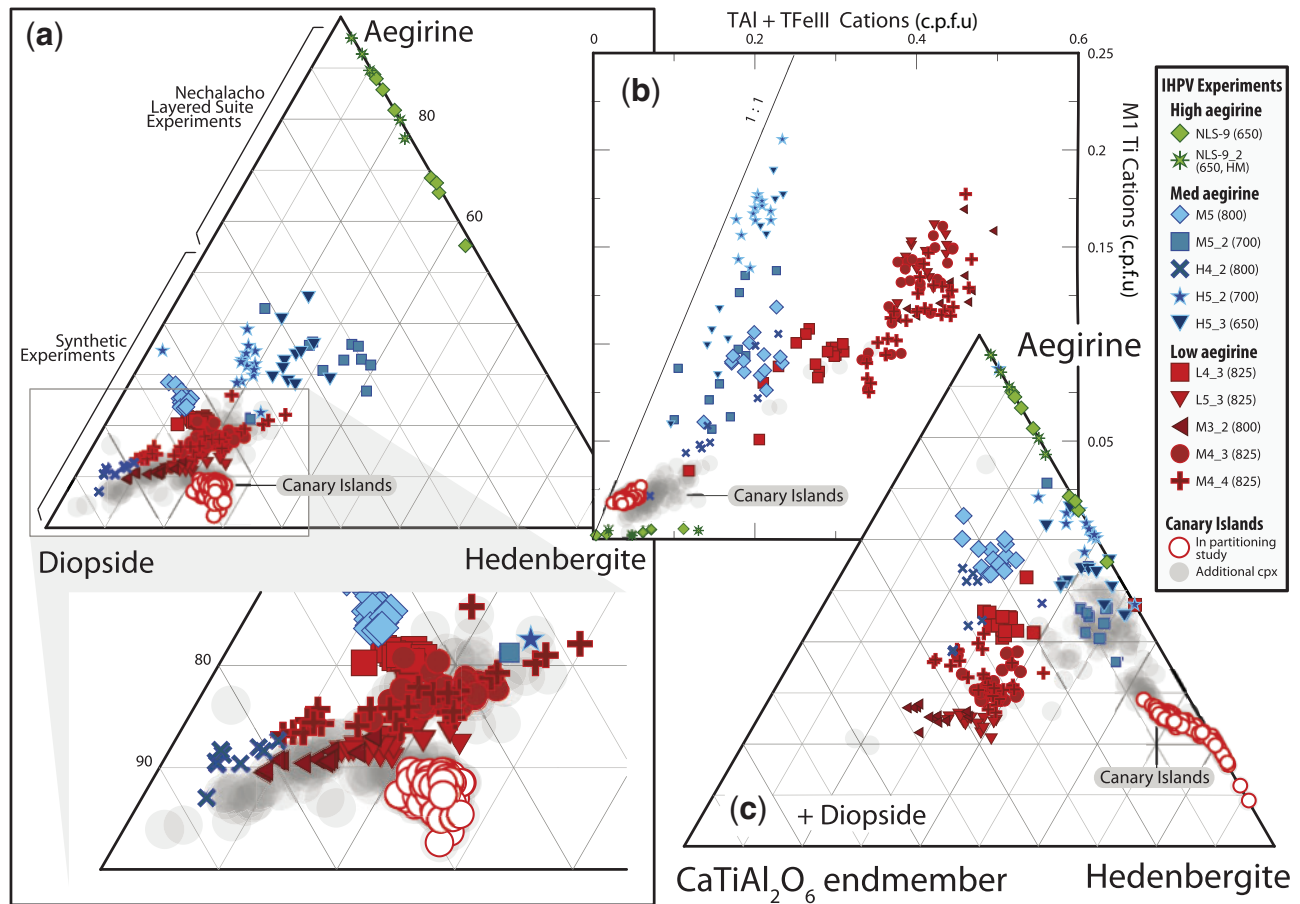
Fig. 4. Major element composition diagrams for experimental and Canary Islands clinopyroxene. (a) Ternary compositional diagram expressed in terms of diopside, hedenbergite and aegirine end-members, (b) diagram showing $^{VI}M1Ti$ vs ^{IV}TAl and Fe^{3+} contents of the clinopyroxene, and (c) ternary diagram expressed in terms of aegirine, hedenbergite and the theoretical $CaTiAl_2O_6$ end-member (Akasaka & Onuma, 1980). Fe^{2+}/Fe^{3+} within the clinopyroxene was assigned following Droop (1987), then site occupancies and end-member proportions were allocated following Morimoto (1989). End-member proportion calculations are given in Supplementary Data Electronic Appendix 6. The range of clinopyroxene compositions within each experiment record both sector zoning and changes to the composition of the melt during crystal growth, whereby the rims (highest Fe, Na) are in equilibrium with the quenched melt. The rims of this clinopyroxene were preferentially sampled in trace element analyses by LA-ICP-MS.

Islands clinopyroxene on a diopside–hedenbergite–aegirine ternary diagram (Fig. 4a, Table 3 and Supplementary Data Electronic Appendix 1). This low-aegirine group of synthetic clinopyroxene displays a positive correlation between $^{IV}Al + {}^{IV}Fe^{3+}$ (in the ^{IV}T site) and ^{VI}Ti content (in the $^{VI}M1$ site, red, low-aegirine, $Aeg_{5–25}$, Fig. 4b), and notably contain both of these elements at elevated concentration relative to the Canary Islands clinopyroxene ($^{IV}Al + {}^{IV}Fe^{3+} = 0.20–0.49$ c.p.f.u., $^{VI}Ti = 0.07–0.17$ c.p.f.u.). A further subset of synthetic clinopyroxene have higher aegirine contents (blue, med-aegirine, $Aeg_{25–50}$) and show a similar range of Ti contents to the low-aegirine synthetic minerals (0.05–0.18 c.p.f.u.), but a limited range of lower $^{IV}Al + {}^{IV}Fe^{3+}$ contents (0.1–0.25 c.p.f.u., Fig. 4b). Experiments performed on the Nechalacho Layered Suite composition (NLS-9, NLS-9$_{2–HM}$, green, high-aegirine, $Aeg_{55–95}$) reproduced the aegirine–augite to aegirine clinopyroxene from the natural system (Möller & Williams-Jones, 2016) that contain low concentrations of $^{IV}Al + {}^{IV}Fe^{3+}$ (up to 0.14 c.p.f.u.) and almost no Ti or Mg.

The six Canary Islands clinopyroxenes that were selected for determination of mineral–melt partition coefficients are diopside in composition ($Di_{65–71}$, $Aeg_{3–10}$ $Hd_{21–28}$), with most crystals containing about 0.05 c.p.f.u. $^{IV}Al + {}^{IV}Fe^{3+}$ and 0.02 c.p.f.u. ^{VI}Ti (Fig. 4b). These minerals are free from melt inclusions, suggesting slow rates of crystal growth (Kennedy et al., 1993, Fig. 1). Chemical zonation, if present, is of a similar magnitude to the analytical precision of our electron microprobe, indicating that pressure, temperature and melt composition remained stable during crystal growth (Fig. 1). Trace element abundances within these Canary Islands clinopyroxenes show core-to-rim variations of about 1–5% relative, with larger variations in element abundance associated with sector zoning than with concentric growth zoning (Supplementary Data Electronic Appendix 1).

In contrast our experimental clinopyroxene displays systematic, albeit minor compositional variation between their cores and rims; this variation recording changes to melt composition during growth of these
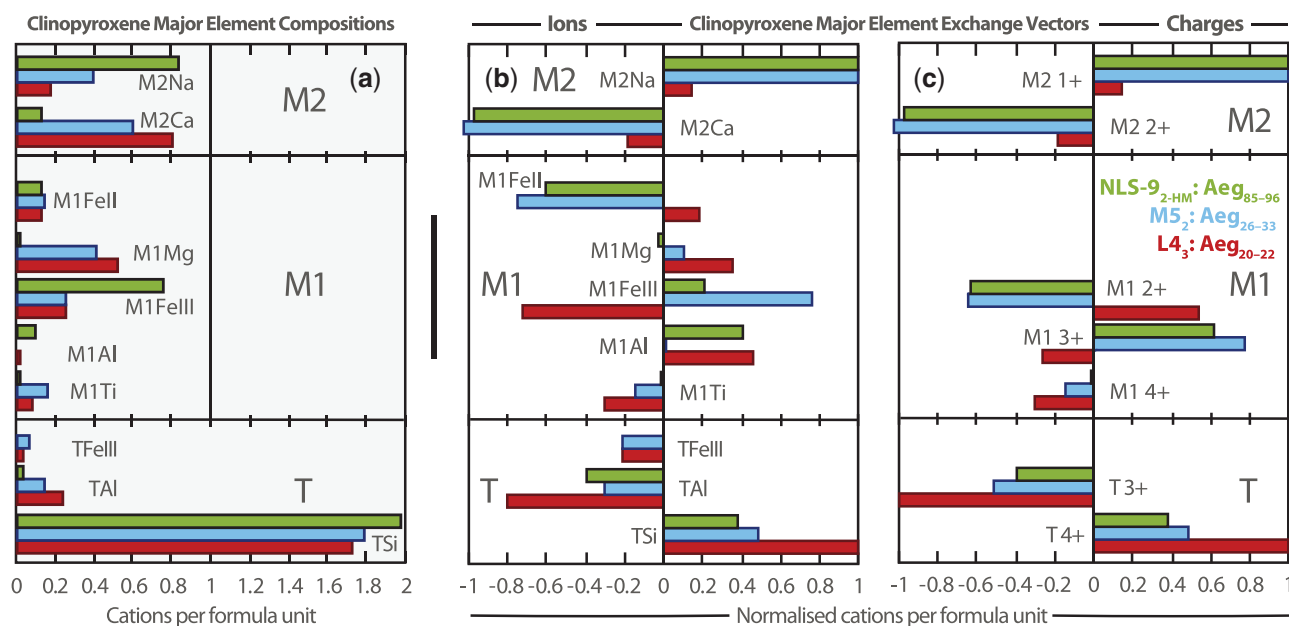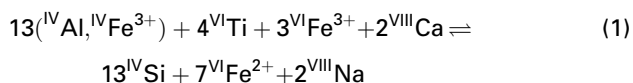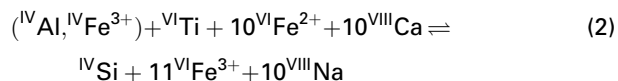
Fig. 5. Bar charts showing clinopyroxene composition and major element exchange mechanisms for three experiments representative of high- (green), medium- (blue) and low-aegirine (red) clinopyroxene. (a) Clinopyroxene major element compositions are expressed as cations per six-oxygen formula unit, (b) exchange mechanisms grouped by ions, (c) grouped by charges. Methods used to calculate these exchange mechanisms are in the caption of Supplementary Data Fig. S4.

crystals (e.g. Fig. 3; cf. Adam *et al.*, 1993; Blundy & Dalton, 2000; Dygert *et al.*, 2014). The systematics of crystal–chemical zonation both within individual experimental charges and within groups of experiments reveal major element exchange vectors between the clinopyroxene and the melt. Three major element exchange mechanisms correspond to the low- (Aeg_{5-25}), medium- (Aeg_{25-50}) and high- (Aeg_{55-95}) aegirine compositional domains defined above (Figs 4b, 5 and Supplementary Data Fig. S4).
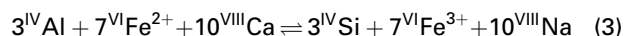
For the low-aegirine series;

$$13(^{IV}Al, ^{IV}Fe^{3+}) + 4^{VI}Ti + 3^{VI}Fe^{3+} + 2^{VIII}Ca \rightleftharpoons \quad (1)$$
$$13^{IV}Si + 7^{VI}Fe^{2+} + 2^{VIII}Na$$

For the medium-aegirine series;

$$(^{IV}Al, ^{IV}Fe^{3+}) + ^{VI}Ti + 10^{VI}Fe^{2+} + 10^{VIII}Ca \rightleftharpoons \quad (2)$$
$$^{IV}Si + 11^{VI}Fe^{3+} + 10^{VIII}Na$$

and for the high-aegirine series;

$$3^{IV}Al + 7^{VI}Fe^{2+} + 10^{VIII}Ca \rightleftharpoons 3^{IV}Si + 7^{VI}Fe^{3+} + 10^{VIII}Na \quad (3)$$

As the aegirine content of clinopyroxene increases, substitutions at the ^{IV}T site become relatively less important than exchanges at the $^{VI}M1$ and $^{VIII}M2$ sites (Fig. 5). At the $^{VI}M1$ site, the importance of Ti substitution for ions of 2+ and 3+ valence also decreases with increasing aegirine content in the clinopyroxene. In low-aegirine clinopyroxene, the concentration of 3+ ions at the $^{VI}M1$ site is negatively correlated with X_{Na}^{M2}, whereas in medium- and high-aegirine clinopyroxene, the $^{VI}M1$ site takes progressively more 3+ ions as X_{Na}^{M2} increases. Substitutions of ^{VIII}Ca for ^{VIII}Na are relatively

unimportant in low-aegirine clinopyroxene, but play a large role in medium- and high-aegirine exchange vectors.

The interdependent nature of clinopyroxene compositional terms provides a link between established compositional influences on trace element partitioning and those that are not traditionally considered (e.g. the ^{IV}Al content of low-aegirine cpx will be positively correlated with fO_2 due to $^{VI}Fe^{3+}$ interdependency; essenite substitution; Eqn 1; cf. Mollo & Vona, 2014). Furthermore, not all of the ^{VIII}Na in the clinopyroxene is charge balanced by $^{VI}Fe^{3+}$; some is charge balanced by $^{VI}Ti^{4+}$ (Eqns 1, 2; cf. Flower, 1974). The latter effect correlates positively with the alkalinity of the starting compositions and may explain why *D* values for HFSE do not vary consistently with ^{IV}Al (Fig. 7).

DISCUSSION

The effect of chemical heterogeneity on apparent partition-coefficients

During our experiments, crystals of clinopyroxene were grown directly from unseeded glasses and the run temperature was approached from super-liquidus conditions. No attempts were made to reverse these experiments by re-equilibrating crystals and liquids with deliberately mismatched trace element concentrations because of the slow diffusion of most elements through the clinopyroxene structure (Van Orman *et al.*, 2001; Cherniak & Dimanov, 2010). As a result of this slow diffusion all experimental clinopyroxene preserves subtle concentric compositional growth zonation, generated as the cores of the grains become chemically
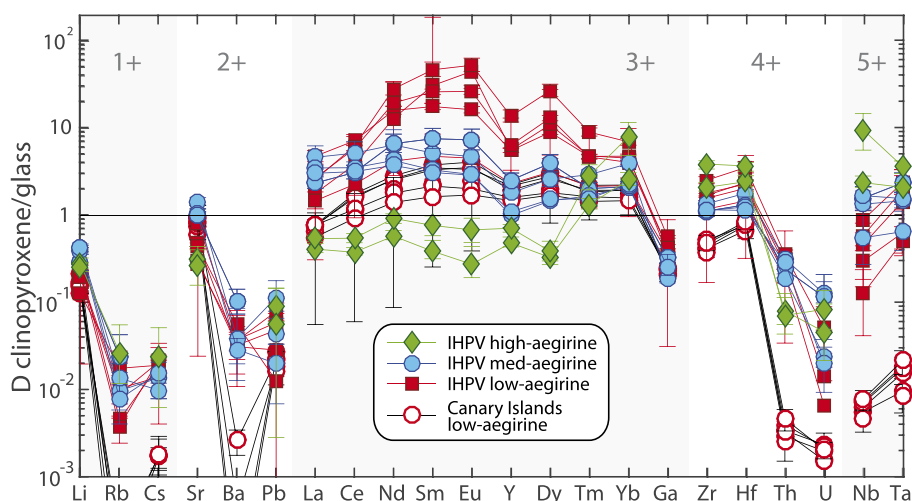
Fig. 6. Diagram of trace element partition-coefficients between clinopyroxene and silicate melt, as determined from internally heated pressure vessel experiments (n = 11; low-, medium- and high-aegirine types) and from clinopyroxene–glass pairs from Tenerife, Canary Islands (n = 6; low-aegirine type). Uncertainties on the partition-coefficients are at the 1σ level.

isolated from the melt during growth (see Fig. 3, Supplementary Data Fig. S3 and Supplementary Data Electronic Appendix 7). Sector zonation is also observed for some clinopyroxene and is associated with larger compositional differences; otherwise the major and trace element concentrations are generally uniform in the quenched melt and mineral phases (Supplementary Data Electronic Appendix 1).

Given the presence of growth zoning, only the crystal rims record true chemical equilibrium with the adjacent melt, and partition coefficients should, therefore, be determined from rim compositions. Unfortunately, in experimental studies, trace element analyses of crystal rims are rarely possible because the mineral grains are commonly comparable in size to the effective beam size of laser-ablation or SIMS systems ($\sim 10 - 20\,\mu m$), as is the case here. We quantify the departure of our apparent partition coefficients, calculated using bulk crystal compositions, from the true values based on the equilibrium clinopyroxene rim compositions using high-resolution Ce-transects measured by EPMA (Supplementary Data Electronic Appendix 4). The transects cross seven experimental clinopyroxene from three experiments, each crystallized to varying degrees, with Ce as a proxy for the compatible elements. Based on these transects, apparent clinopyroxene–melt partition coefficients for compatible elements are offset from equilibrium (rim Ce) to higher values by 4–12% (apparent D values are calculated using bulk crystal Ce contents, expressed as the transect median Ce, see Supplementary Data Electronic Appendix 4). These values are not correlated with the degree of crystallization in the three experiments, however the highest values are found for the largest clinopyroxene crystals (c.100 μm) and in these, because of their size, we were able to avoid the cores in the analyses by LA-ICP-MS. The 12% deviation thus represents a maximum estimate of the bias from equilibrium in the partition

coefficients. Moreover, at the low degrees of crystallization of our experiments median incompatible element concentrations in clinopyroxene are more subtly offset from equilibrium values than compatible elements because their concentration in the melt varies less during crystallization (see Supplementary Data Electronic Appendix 7).

Most importantly, the systematic positive bias in compatible D values observed here is small relative to the variation in partition coefficients for our complete sample set, as well as that of literature values (e.g. Fig. 7 below). Our experimentally-derived apparent partition coefficients plot on trends with clinopyroxene major element composition defined by literature data (Fig. 7). Because the potential bias in our apparent partition coefficients is not significant relative to the variation in the full dataset, no bias correction factor has been applied to our data. A limited deviation from equilibrium is further evidenced by a lack of correlation between the composition and the size of the analysed clinopyroxene, and the small variability in clinopyroxene and melt compositions within each experiment.

Attainment of equilibrium in the Canary Islands rocks

The Canary Islands trace element partition coefficients presented here were determined from euhedral, blade-shaped crystals free of melt inclusions and chemical zonation. The corresponding quenched melt was in direct contact with these crystals and shows no zonation in backscattered electron images (Fig. 1). While equilibrium conditions are challenging to confirm for a natural volcanic system, the euhedral forms, chemical homogeneity of crystals, and congruency between samples from separate eruptions suggest that the crystals grew in a stable environment, and were not subject to chemical or physical perturbations during growth (Figs 1 and 4). In the case of these Canary Islands clinopyroxene,
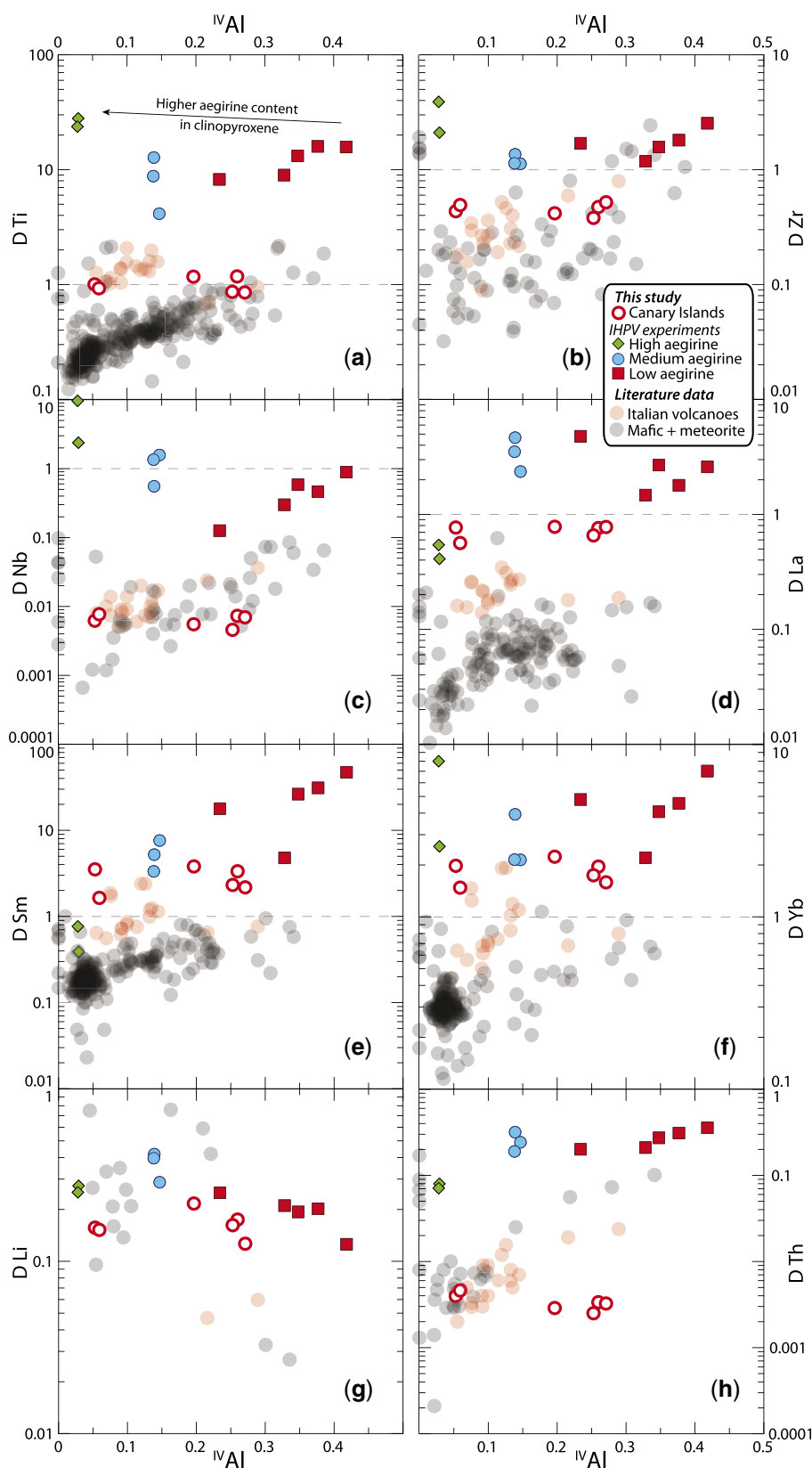
Fig. 7. Clinopyroxene–melt trace element partition coefficients vs the ^{IV}Al content of clinopyroxene (c.p.f.u.). Elements shown are the HFSE (Ti, Zr, Nb), REE (La, Sm, Yb) and TE (Li, Th). Literature values (n = 411), including those from potassic Italian volcanoes (red), are from the compilation of Bédard (2014) and Mollo *et al.* (2016). Supplementary Data Fig. S5 shows similar diagrams with X_{Na}^{M2} in place of ^{IV}Al.

the entire mineral is interpreted to be in chemical equilibrium with the adhered quenched melt.

Trace element partitioning

Apparent Nernst partition coefficients (D values) and their uncertainties were calculated as mass concentration ratios between clinopyroxene and coexisting glass (Table 4 and Supplementary Data Electronic Appendix 1). Three markedly different behaviours of rare earth element partitioning are observed in the experiments (Fig. 6). These depend on the aegirine concentration in the clinopyroxene and match the major element exchange vector domains discussed above. Low-aegirine experimental clinopyroxene (Aeg_{5-25}) prefer the MREE; medium-aegirine clinopyroxene (Aeg_{25-50}) shows a similar behaviour, save for higher LREE partition coefficients, whereas high-aegirine clinopyroxene (Aeg_{55-95}) strongly prefer HREE and show incompatible behaviour for the light and middle REE. The experimental REE partition coefficients are 0·3–53, typically 2–6, with minima for LREE and MREE in high-aegirine clinopyroxene (Fig. 6). Apparent REE partition coefficients determined from our experiments are positively correlated with the ^{IV}Al content of the clinopyroxene and are an order of magnitude higher than most literature values, the majority of which were determined for more mafic compositions (e.g. Fig. 7e). The Canary Islands clinopyroxene and low-aegirine experiments show similar inter-element partitioning systematics for the REE, with absolute values for the Canary Islands partition coefficients of about one order of magnitude lower (Fig. 6).

The high field-strength elements (HFSE) Ti, Zr, Hf, Nb and Ta are compatible to slightly incompatible in the experimental clinopyroxene, and typically 1–2 orders of magnitude less compatible in the Canary Islands clinopyroxene (Fig. 7a–c). D_{HFSE} for the low-aegirine experiments and Canary Islands rocks plot on trends with the ^{IV}Al content of clinopyroxene, as defined by literature data from Italian volcanoes (Wood & Trigila, 2001; Fedele et al., 2009; Mollo et al., 2013, 2016). In our medium- and high-aegirine experiments D_{HFSE} values are not correlated with the ^{IV}Al (or ^{VI}Ti) content of clinopyroxene, consistent with a distinct incorporation mechanism for these elements relative to the low-aegirine experiments. Major element exchange mechanisms derived from our experiments suggest that HFSE (e.g. Ti) incorporation is charge balanced by substitution of ^{VIII}Ca for ^{VIII}Na, as well as by ^{IV}Si for ^{IV}Al, the relative importance of the former mechanism increasing with the alkali content of the system (cf. Eqn. 1–2). A weak positive correlation between X_{Na}^{M2} and D_i for the HFSE Ti, Zr and Nb is consistent with this mechanism (Fig. 7 & Supplementary Data Fig. S5; cf. Flower, 1974).

Partition coefficients for the large-ion lithophile elements K, Sr, Pb are positively correlated with X_{Na}^{M2} in the low- and medium-aegirine clinopyroxene, but are lower in high-aegirine clinopyroxene (Fig. 6; Supplementary Data Electronic Appendix 1). The Rb, Cs and Ba partition

coefficients have a high uncertainty and are maximum estimates owing to concentrations of these elements in the clinopyroxene being close to the LA-ICP-MS detection limit. Lithium is incompatible ($D_{Li} = 0·1–0·4$) in both Canary Islands and experimental clinopyroxenes and, like Sr and Pb, becomes more compatible with increasing aegirine content in the clinopyroxene, plateauing at $X_{Na}^{M2} = 0·4$ and decreasing thereafter (Supplementary Data Fig. S5g). The actinides U and Th show contrasting partitioning behaviour; the former showing no correlation with aegirine content in the clinopyroxene, the latter becoming more incompatible with increasing aegirine content (Fig. 7h). The U and Th partition coefficients for our Canary Islands samples are similar to those for the Italian volcanoes, and are 1–2 orders of magnitude more incompatible relative to the experimental clinopyroxene.

In polymerised silicate melts ($NBO/T < 0·49$), the melt structure can impart a significant influence on trace element partitioning behaviour (Gaetani, 2004; Huang et al., 2006; Schmidt et al., 2006). However, in the depolymerised peralkaline melts studied here apparent partition coefficients are not correlated with NBO/T, except for D_{Sr} that shows a weak positive correlation (Fig. 8). NBO/T could not be calculated for our Canary Islands compositions because the water content of the melt prior to quench is not known.

Fits to the lattice-strain model

The equilibrium partitioning of trace elements between minerals and melts is largely controlled by the structure of the crystal lattice, its elasticity (Onuma et al., 1968; Kumazawa, 1969; Weidner & Vaughan, 1982) and its ability to accommodate an excess or deficit in charge (Blundy et al., 1998; Hanchar et al., 2001; Wood & Blundy, 2001; Corgne & Wood, 2005). The lattice-strain model provides a framework in which the influence of these variables on partitioning behaviour can be quantified, and thus predicted under conditions bracketed by a calibrating data set (Onuma et al., 1968; Blundy & Wood, 1994; Wood & Blundy, 2014).

Most trivalent ions, including the REE and Y enter the M2 site of clinopyroxene, which is 6- or 8-coordinated (Deer et al., 1992). Smaller trivalent ions, including Al, Cr, Ga, Sc, and, in the case of Fe-rich clinopyroxene, the HREE, may enter the smaller $^{VI}M1$ site (Olin & Wolff, 2010; Reguir et al., 2012; Bédard, 2014). The high field-strength elements Ti, Zr, Hf, Nb and Ta are typically hosted by the $^{VI}M1$ site (Hill et al., 2000, 2011; Dygert et al., 2014).

To investigate systematics in D_i values and the mechanisms by which trace elements are incorporated into clinopyroxene, element partitioning behaviour was explored in the light of lattice-strain theory, quantitatively described by the lattice-strain equation:

Table 4: Clinopyroxene–melt trace-element-partition coefficients for representative internally heated pressure vessel experiments and a natural phenocryst–glass pair

	Internally-heated pressure-vessel experiments										Tenerife	
	$L4_3$		$M3_2$		$M5_2$		$H5_3$		NLS-9		16-07 px4 LMB	
	D	σ	*D*	σ	*D*	σ	*D*	σ	*D*	σ	*D*	σ
Li	0·250	0·016	0·126	0·009	0·419	0·034	0·427	0·024	0·274	0·029	0·157	0·021
Ga	0·364	0·022	0·567	0·020	0·190	0·022					0·216	0·020
Rb	0·005	0·002	0·018	0·003	0·010	0·006	0·013	0·002	0·026	0·015	0·000	0·000
Sr	0·828	0·045	0·282	0·024	1·433	0·111	0·997	0·091	0·321	0·045	0·732	0·293
Y	5·577	0·302	13·784	1·949	1·814	0·236	1·102	0·060	0·482	0·048	2·183	0·232
Zr	1·699	0·082	2·537	0·222	1·361	0·089	1·164	0·083	2·102	0·196	0·434	0·047
Nb	0·126	0·085	0·889	0·258	0·554	0·280	1·688	0·196	2·382	0·294	0·0062	0·0004
Cs	0·019	0·003	0·019	0·003	0·014	0·006	0·010	0·002	–	–	0·001	0·001
Ba	0·0364	0·0087	0·0373	0·0152	0·0388	0·0261	0·0288	0·0091	–	–	0·00004	0·00004
La	4·787	0·646	2·591	0·240	4·658	0·962	3·049	0·132	0·410	0·037	0·769	0·071
Ce	7·199	0·756	6·229	0·646	5·199	1·073	3·190	0·129	0·377	0·028	1·591	0·120
Nd	16·105	1·537	28·430	4·210	6·454	1·630	3·759	0·147	0·579	0·054	2·632	0·155
Sm	17·843	1·414	47·245	7·699	5·215	1·293	3·113	0·137	0·388	0·070	3·522	0·421
Eu	16·403	1·341	53·195	8·181	4·743	1·132	2·900	0·133	0·275	0·082	3·372	0·196
Dy	9·027	0·537	27·082	3·925	2·619	0·460	1·521	0·073	0·329	0·057	2·798	0·220
Tm	4·773	0·261	9·067	0·903	2·937	0·279	1·567	0·097	1·330	0·145	1·846	0·182
Yb	4·797	0·249	7·015	0·600	3·937	0·296	2·281	0·152	2·564	0·346	1·978	0·186
Hf	2·385	0·162	3·556	0·472	1·802	0·118	1·141	0·123	2·443	0·275	0·769	0·065
Ta	0·496	0·152	2·3694	0·6244	0·6502	0·2545	1·5654	0·2337	2·1082	0·1764	0·0153	0·0013
Pb	0·079	0·017	0·0587	0·0152	0·1142	0·0349	0·0199	0·0130	0·0884	0·0280	0·0203	0·0040
Th	0·201	0·034	0·3565	0·0419	0·3172	0·0321	0·2892	0·0239	0·0798	0·0240	0·0040	0·0003
U	–	–	0·0512	0·0331	0·1261	0·0272	0·0196	0·0103	0·0460	0·0245	0·0022	0·0003

$$D_i^{mineral/melt} = D_0 \, \exp\left[\frac{-4\pi E_s N_a}{RT}\left(\frac{r_0}{2}(r_0 - r_i)^2 - \frac{1}{3}(r_0 - r_i)^3\right)\right]$$
(4)

where r_0 is the ideal radius for the lattice site, E_s is the Young's modulus (i.e. the lattice site stiffness in GPa), D_0 is the strain-free partition coefficient, N_a is Avogadro's number, R is the gas constant, T is temperature in Kelvin, and r_i is the ionic radius of the element in question, all radii in Å. We focused on 3+ ions that cover a wide range of radii and fitted lattice-strain parameters for both the $^{VI}M1$ and $^{VIII}M2$ sites of clino-pyroxene (Fig. 9):

$$D_i^{cpx/melt} = D_0^{M2} \, \exp\left[\frac{-4\pi E_s^{M2} N_a}{RT}\left(\frac{r_0^{M2}}{2}(r_0^{M2} - r_i)^2 - \frac{1}{3}(r_0^{M2} - r_i)^3\right)\right]$$

$$+ D_0^{M1} \, \exp\left[\frac{-4\pi E_s^{M1} N_a}{RT}\left(\frac{r_0^{M1}}{2}(r_0^{M1} - r_i)^2 - \frac{1}{3}(r_0^{M1} - r_i)^3\right)\right]$$
(5)

Parabolae for 3+ ions were fitted for the $^{VI}M1$ and $^{VIII}M2$ sites using the REE, Ga and Al assigned to the $^{VI}M1$ site of clinopyroxene (Fig. 9a). Fits are weighted based on uncertainties for the element partition coefficients. HREE have higher element partition coefficients than can be predicted by substitution into the $^{VIII}M2$ site, hence were fitted with ionic radii for six fold coordination into the $^{VI}M1$ site (Olin & Wolff, 2010; Reguir et al., 2012; Bédard, 2014). Lattice-strain parameters as obtained from fits to the data are shown in Figs. 9–12 and Supplementary Data Electronic Appendix 1.

In some low-aegirine experiments and the Canary Islands rocks, lattice-strain fitting for 3+ ions at the $^{VI}M1$ site was not possible, because too few HREE partitioned onto the $^{VI}M1$ site of this clinopyroxene. Here, we chose to fit only lattice-strain parameters for the $^{VIII}M2$ site, or fix D_0^{3+} values for the $^{VI}M1$ site to match those for the $^{VIII}M2$ site, and fit only the r_0 and E_s parameters for the $^{VI}M1$ site (Supplementary Data Electronic Appendix 1). Fitting of element partitioning data for 1+, 2+ and 4+ ions was less successful owing to sparse coverage of suitable radii and detection limit issues for some elements. Partition coefficients for 1+, 2+, and 4+ elements follow radius- and charge-dependent trends consistent with lattice-strain theory and reported effects of charge on lattice-strain parameters (Fig. 9b; e.g. Hazen & Finger, 1979; Law et al., 2000; Adam & Green, 2006).

Effects of composition on ideal site size, r_0

As the composition of clinopyroxene shifts from augite toward aegirine, the size of the $^{VI}M1$ and $^{VIII}M2$ sites, or strain-free radii (r_0), should diverge following the sizes of the major element cations on these sites. Lattice-strain fits for 3+ cations indicate expansion of the $^{VIII}M2$ site between low and medium-aegirine clinopyroxene, with $r_{0,M2}^{3+}$ correlating well with Na replacing Ca (Figs 9 and 10). Expansion of the $^{VIII}M2$ site stalls at $r_{0,M2}^{3+} \approx 1.12$ Å and $X_{Na}^{M2} \approx 0.4$, changing little in size between medium and high-aegirine clinopyroxene. We suggest that this is a 'saturation effect', whereby the smaller ions in the ^{IV}T and $^{VI}M1$ sites prevent further expansion of the $^{VIII}M2$ site as additional R_{M2}^+ (any cation of 1+ valence) is added to the clinopyroxene. For the $^{VI}M1$ site of clinopyroxene, strain free radii for R^{3+} cations indicate expansion between low and medium-aegirine
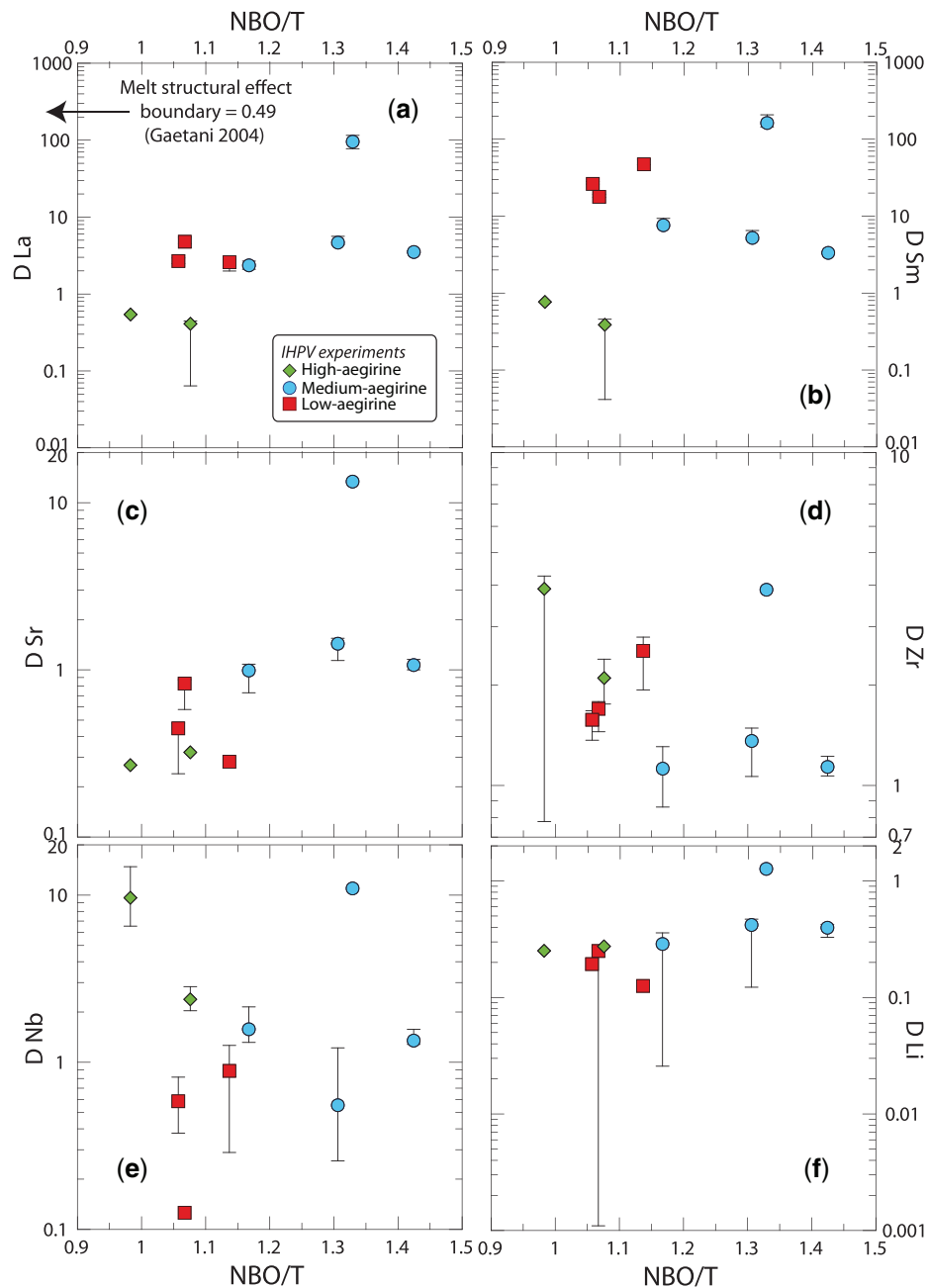
Fig. 8. Diagrams of clinopyroxene–melt trace element partition coefficients for the IHPV experiments as a function of NBO/T of the quenched melt. NBO/T was calculated following Mysen *et al.* (1985) with melt Fe oxidation state assigned following Kress & Carmichael (1991) and the water content of the melt estimated by difference from 100% major element oxides.

clinopyroxene and contraction between medium and high-aegirine clinopyroxene (Figs 9 and 10). These trends broadly follow the substitution of Mg^{2+} for Fe^{2+}, then Fe^{2+} for Fe^{3+} with increasing aegirine content in the clinopyroxene.

The effect of cation charge on the D_0 parameter

The D_0 parameter of the lattice-strain model describes ideal, strain-free partitioning and tracks the solubility of an ideal cation in the mineral with changing pressure, temperature and the bulk composition of the system

(Wood & Blundy, 2014). D_0, therefore, correlates with the major element composition of the clinopyroxene, as well as that of the melt (e.g. Jd-melt, Jd-DiHd and CaTS-DiHd exchanges have been shown to control REE incorporation in cpx; Putirka, 2008; Wood & Blundy, 2014; Mollo *et al.*, 2017). Incorporation of trace elements of a different charge introduces an electrostatic penalty that leads to a lower D_0 for that charge (Wood & Blundy, 2001, 2003).

The average charge of major elements on the $^{VIII}M2$ site of clinopyroxene decreases from $2+$ to $1+$ on the compositional join between Ca-rich diopside and
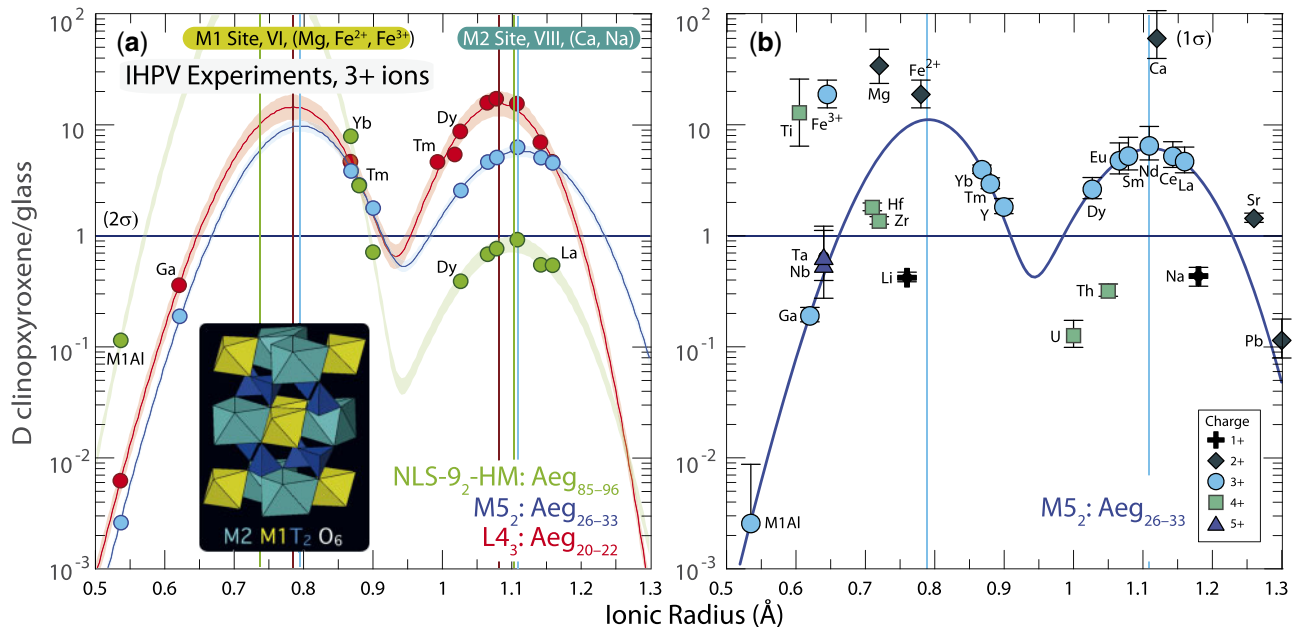
Fig. 9. Onuma diagrams for clinopyroxene–melt partitioning of R^{3+} cations, as determined from internally-heated pressure vessel experiments. Parabolae are non-linear, weighted least-squares fits to the element partitioning data following the lattice-strain model of Blundy & Wood (1994). Shaded uncertainty envelopes, determined via bootstrapping, are at the 2σ level. (a) Representative fits to $3+$ ion partitioning behaviour with examples for low- (red), medium- (blue) and high-aegirine (green) clinopyroxene experiments. Vertical coloured lines indicate ideal ionic radii (r_0^{3+}) of $^{VI}M1$ and $^{VIII}M2$ sites. (b) Measured partition-coefficients for ions of $1+$, $2+$, $4+$ and $5+$ charges that are consistent with the lattice-strain model. Uncertainties are shown at the 1σ level. R^{3+} ions were assigned to 6 or 8 fold coordination (Shannon, 1976), based on minimal residuals in the fit of parabolae (cf. Olin & Wolff, 2010). Y was not included in the fitting routine for R^{3+} ions because of mass fractionation effects (ibid.). Fitted lattice-strain parameters are given in Table 4.
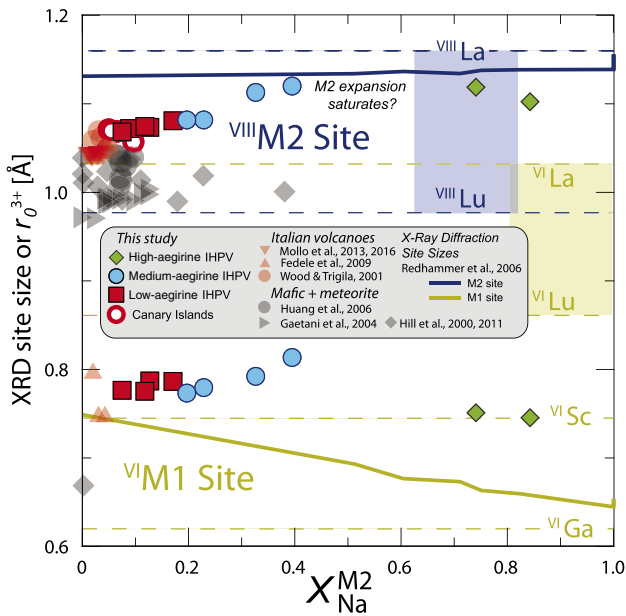

Fig. 10. Diagram showing variation of ideal ionic radius r_0^{3+} with XNa for the $^{VI}M1$ and $^{VIII}M2$ sites of clinopyroxene. Shown for comparison are single crystal x-ray diffraction data from the hedenbergite–aegirine compositional join (heavy solid lines, from Redhammer et al., 2006). Shaded boxes represent the range of ionic radii for rare earth elements in VI and VIII co-ordination, with labelled fine dashed lines indicating selected ionic radii (Shannon, 1976). Literature data for Italian volcanoes are from Wood & Trigila (2001); Fedele et al. (2009); Mollo et al. (2013, 2016) and for mafic systems from Hill et al. (2000, 2011); Gaetani (2004); Huang et al. (2006).

Na-rich aegirine. Consequently, the electrostatic penalty for substituting a REE^{3+} cation into the clinopyroxene $^{VIII}M2$ site is increased (Fig. 11c). Conversely, as the average charge on the $^{VI}M1$ site of clinopyroxene increases from $2+$ toward $3+$ in end-member aegirine, the electrostatic penalty incurred when substituting REE^{3+} cations onto the $^{VI}M1$ site is reduced (Fig. 11d) $D_{0,M1}^{3+}$ consequently increases by an order of magnitude between our medium-aegirine and high-aegirine experimental clinopyroxene, an effect that when combined with the shrinking $^{VI}M1$ site size, leads to strong fractionation of the HREE (Figs 9 and 11d).

A positive correlation between ^{IV}Al and partition coefficients for highly charged trace elements has been extensively documented in studies on clinopyroxene (Lundstrom et al., 1994; Gaetani & Grove, 1995; Blundy et al., 1998; Francis & Minarik, 2008; Hill et al., 2011; Mollo et al., 2016). The low-aegirine experimental clinopyroxene and most of the Canary Islands rocks extend trends defined by clinopyroxene from mafic systems (Figs 7 and 11a), whereas the remainder of the experimental data set and Canary Islands rocks show element partitioning behaviour similar to Italian volcanoes (Wood & Trigila, 2001; Fedele et al., 2009; Mollo et al., 2016), confirming that an ^{IV}Al-controlled substitution mechanism for REE extends to peralkaline conditions (Figs 7 and 11a).

D_0^{3+} parameters for the $^{VI}M1$ site are strongly correlated with those for the $^{VIII}M2$ site, except at aegirine
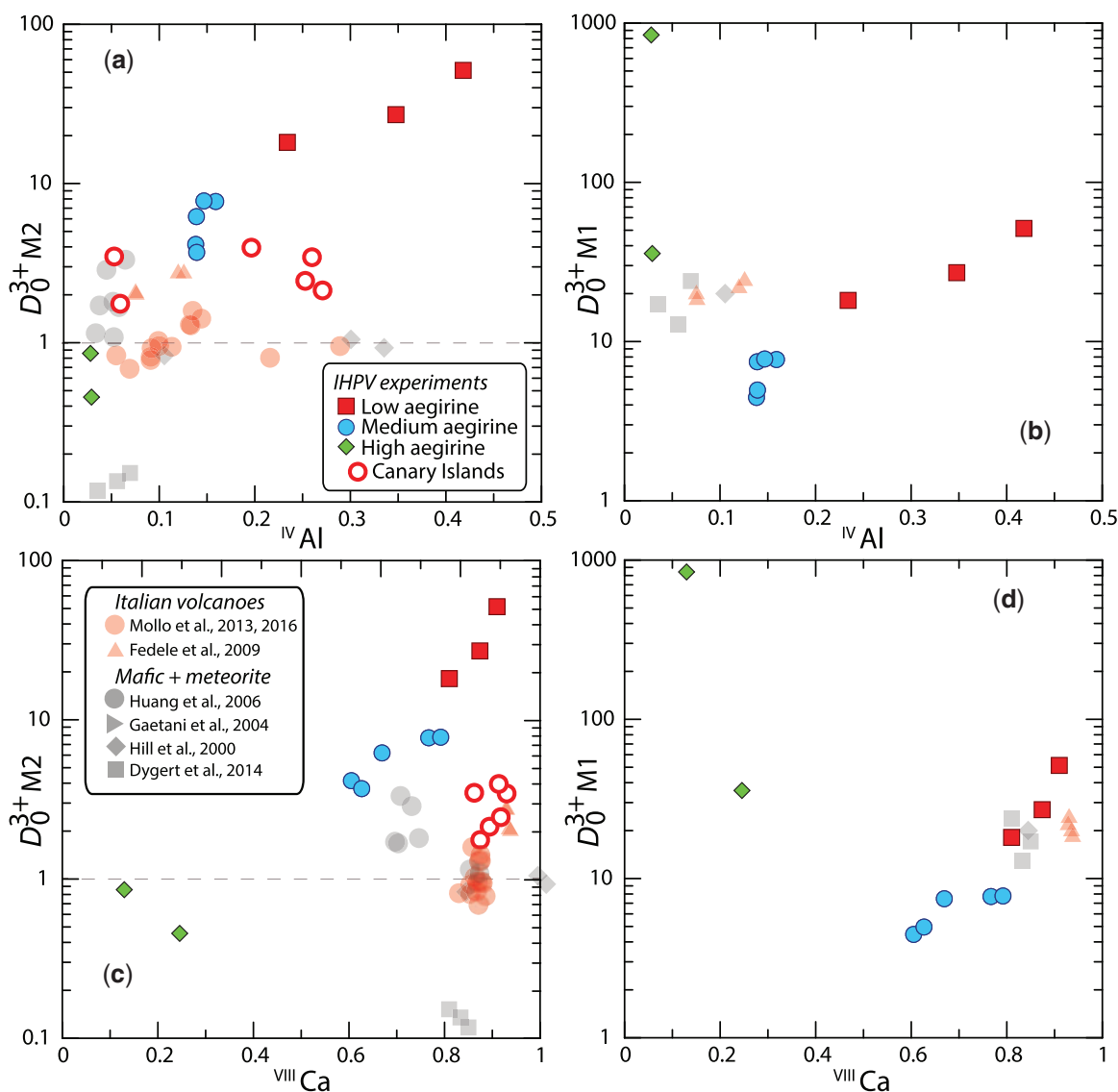
Fig. 11. Diagrams of strain-free partition-coefficients (D_0) for 3+ ions into clinopyroxene vs clinopyroxene major element composition. (a, c) are for the ^{VIII}M2 site, and (b, d) are for the ^{VI}M1 site. The diagrams show that variability in partitioning behaviour is highly dependent on mineral composition, and that incorporation of trace elements into aegirine-rich clinopyroxene cannot be explained well by the same mechanisms as for mafic systems (c). Literature data for element partitioning in mafic + meteorite and Italian volcano compositions are from the compilations of Bédard (2014) and Mollo *et al.* (2016). 1σ uncertainties on the fitted lattice strain parameters are smaller than the symbol sizes.

concentrations exceeding 50 mol %. Similarities to ^{VIII}M2 partitioning behaviour likely reflect the dominance of ^{IV}T site substitution mechanisms in augite clinopyroxene. In the high-aegirine clinopyroxene, ^{IV}T site substitutions become less important as the ^{IV}T sites become saturated with Si^{4+} (Fig. 5). Here, the dominant ion on the ^{VI}M1 site is Fe^{3+}, the replacement of which by R^{3+} trace elements does not introduce a charge penalty. Consequently $D^{3+}_{0,M1}$ values for aegirine are higher than for more magnesian clinopyroxene.

An element partitioning model extending to aegirine clinopyroxene

Partition coefficients vary systematically with the physicochemical conditions of natural and synthetic magmas

(cf. Wood & Blundy, 2003). A number of models have been presented that describe these systematics for clinopyroxene–melt partitioning (Wood & Blundy, 1997, 2001; Hill *et al.*, 2011; Sun & Liang, 2012; Yao *et al.*, 2012; Bédard, 2014; Dygert *et al.*, 2014; Mollo *et al.*, 2016, 2018). The majority of these models are based on lattice-strain theory and predict how the lattice parameters r_0, E_s, and D_0 vary with composition, temperature and pressure. This semi-thermodynamic approach theoretically permits calculation of partition coefficients for any trace element, at any set of $P - T - X$ conditions. In reality, all models have a limited applicable range, as restricted by the input data set. Because existing partitioning models do not reproduce the high $r^{3+}_{0,M2}$ values for clinopyroxene with aegirine content that exceed
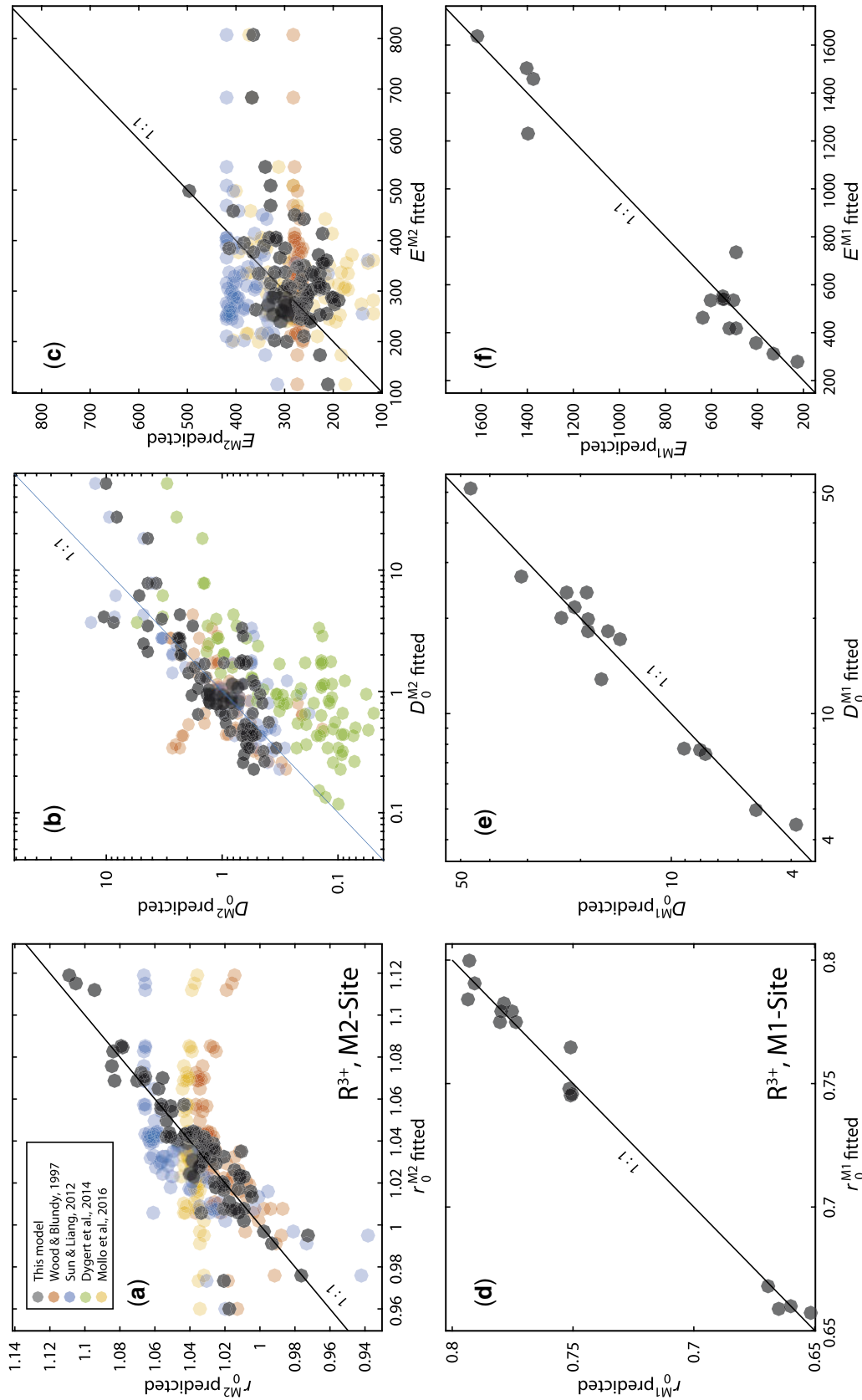
Fig. 12. Fitted *vs* predicted model values for lattice-strain parameters for the ^{VIII}M2 and ^{VI}M1 sites of clinopyroxene. Empirical partitioning models were generated via a stepwise multiple linear regression procedure following a hierarchical forward selection criterion with switching. The models for r_0^{M1} and EM^1 are calibrated for use all the way to end-member aegirine, whereas the model for the D_0^{M1} term is only calibrated for use up to $\sim$Aeg$_{50}$. Model equations are in the main text, with coefficients given in Table 5.

Table 5: Coefficients for the prediction of lattice-strain parameters for R^{3+} ions between clinopyroxene (^{VI}M1 and ^{VIII}M2 sites) and silicate melt

Model for r_0, ^{VIII}M2 site (n = 82)			Model for r_0, ^{VI}M1 site (n = 16)		
Parameter	Coefficient	σ	Parameter	Coefficient	σ
Intercept	1·01	0·02	Intercept	0·79	0·03
^{VI}M1Ti	0·16	0·05	P [GPa]	−0·017	0·005
^{VI}M1Al - ^{VI}M1Fe^{3+}	−0·03	0·01	^{VIII}M2Mg	−0·48	0·06
^{VIII}M2Ca	0·09	0·02	^{VI}M1Fe^{3+}	0·14	0·03
^{VIII}M2Na	0·14	0·02	^{VIII}M2Ca	−0·05	0·02
T [K]	−4·5E-05	1·2E-05			
R^2		0·846			0·987
Model for LnD_0, ^{VIII}M2 site (n = 82)			**Model for LnD_0, ^{VI}M1 site (n = 16)**		
Parameter	Coefficient	σ	Parameter	Coefficient	σ
Intercept	4·52	0·91	Intercept	5	1
^{VI}M1Ti	6·8	3	^{IV}TAl	4	0·5
^{VI}M1Al - ^{VI}M1Fe^{3+}	1·6	0·6	^{VI}M1Fe^{2+}	2·6	0·9
^{VIII}M2Fe^{2+}	-3·8	1·3	^{VIII}M2Na	−8	1
T [K]	-0·0035	0·0007	^{VIII}M2Ca	−3	2
^{IV}TAl + ^{IV}TFe^{3+}	2·6	0·8			
R^2		0·647			0·959
Model for E$_s$, ^{VIII}M2 site (n = 79)			**Model for E$_s$, ^{VI}M1 site (n = 18)**		
Parameter	Coefficient	σ	Parameter	Coefficient	σ
Intercept	247	44	Intercept	−2322	298
^{VI}M1Al	-424	144	T [K]	3·2	0·4
^{VI}M1Mg	-285	102	P [GPa]	−408	145
^{VI}M1Ti	-1145	378	^{VI}M1Mg	−800	212
^{VIII}M2Mg	-306	115			
P [GPa]	37	12			
^{IV}TAl + ^{IV}TFe^{3+}	313	102			
XMg	336	102			
R^2		0·348			0·936

Multiple linear regression reports generated during the calibration of these models are available in Supplementary Data Electronic Appendix 5.

50 mol % (Fig. 12a), they cannot accurately predict REE partitioning behaviour for strongly peralkaline systems. We here present a new empirical model calibrated on both our work (n = 16) and existing partitioning data from the literature (n = 75, compilation of Bédard, 2014 and Mollo *et al.*, 2016; Fig. 12; Supplementary Data Electronic Appendix 1) to extend the applicable compositional range for our model. Our calibration database covers a wide range of composition, pressure, temperature and oxygen fugacity (0·0001–3·5 GPa, 650–1345°C, log fO_2 = IW to MH $\approx$ ΔFMQ -5 to +5). Clinopyroxene compositions are XMg 0·031–1, X_{Na}^{M2} 0–0·84 and ^{IV}Al 0–0·49 c.p.f.u. and melt compositions are Mg# (0–100) and XH$_2$O (0–0·38). REE partition-coefficients are D_{La} 0·01–4·79; D_{Sm} 0·02–47·24, and D_{Yb} 0·11–8·00. The majority of partition coefficients in the data set were measured via SIMS or LA-ICP-MS, minimising analytical uncertainty (e.g. from analyses by electron microprobe).

An empirical partitioning model that includes both clinopyroxene and melt parameters has the highest potential for accuracy (e.g. Wood & Blundy, 2014). However, such models cannot be applied in geological scenarios where melt composition cannot be directly measured, for example to the cores of zoned phenocrysts in tephra, or to cumulate systems. Therefore we restrict our model to clinopyroxene compositional terms alone, an approach that is valid because crystallization is a thermodynamically-controlled process and the composition of the melt, and thus its effects on element partitioning are, at least in part, recorded by the major element composition of the clinopyroxene.

The clinopyroxene M2 site
To determine the principal physico-chemical factors that affect element partitioning at the ^{VIII}M2 site of clinopyroxene, a stepwise least-squares multiple linear regression analysis was performed using the lattice-strain parameters r_0^{3+}, D_0^{3+} and E_s^{3+}, temperature, pressure and clinopyroxene composition as inputs. Input parameters were initially examined in binary scatter diagrams to ascertain whether correlations with lattice-strain parameters were linear. If not, interaction compositional terms were added to the initial set of possible fitting parameters that had linear correlations with lattice-strain parameters (e.g. $X_{Al+Fe^{3+}}^T$). Intensive variables for multiple regression models for r_0, D_0 and E_s were introduced following a hierarchical forward selection criterion with switching. Only parameters that were statistically significant at the 95% confidence level were retained, with the largest number of significant terms being eight for E^{M2} (cf. Supplementary Data Electronic Appendix 5).

The resultant empirical model accounts well for changes in lattice-strain parameters over a range of compositions from basalt to peralkaline phonolite, reproducing large r_0^{M2} values typical for sodic clinopyroxene (Fig. 12a; model coefficients in Table 5). Student t-tests show that all of the independent variables included in the models are significant at the 95% confidence level and PRESS R^2 values obtained by repeated random sub-sampling of the dataset (Stevens, 1996) are close to R^2 values calculated by regular methods, indicating that the models are robust and have high predictive power. Full multiple regression reports are available in Supplementary Data Electronic Appendix 5. Equations generated by the multiple linear regression calculations are given below for the $^{VIII}M2$ site, where a_i are the regression coefficients for the respective variables:

$$r_0^{M2} = a_{15} + a_{16}T + a_{17}X_{Al-Fe^{3+}}^{M1} + a_{18}X_{Ti}^{M1} + a_{19}X_{Ca}^{M2} + a_{20}X_{Na}^{M2} \tag{6}$$

$$lnD_0^{M2} = a_1 + a_2T + a_3X_{Al+Fe^{3+}}^{T} + a_4X_{Ti}^{M1} + a_5X_{Al-Fe^{3+}}^{M1} + a_6X_{Fe^{2+}}^{M2} \tag{7}$$

$$E^{M2} = a_7 + a_8P + a_9X_{Al+Fe^{3+}}^{T} + a_{10}X_{Al}^{M1} + a_{11}X_{Mg}^{M1} + a_{12}X_{Ti}^{M1} + a_{13}X_{Mg}^{M2} + a_{14}X_{Mg} \tag{8}$$

The model for r_0^{M2} incorporates compositional controls from the $^{VI}M1$ and $^{VIII}M2$ sites, as well as temperature. Elevated concentrations of large $^{VIII}M2$ cations Ca^{2+} and Na^+ are correlated with large $^{VIII}M2$ sites. Ti^{4+} cations in the neighbouring $^{VI}M1$ site are also correlated with expansion of the $^{VIII}M2$ site, and the concentration of small Al^{3+} minus larger Fe^{3+} on the $^{VI}M1$ site is negatively correlated with r_0^{M2}. The negative correlation between r_0^{M2} and temperature reflects the sum of changes to major element composition that lead to smaller clinopyroxene $^{VIII}M2$ sites at higher temperatures. This compositional effect swamps the minor influence of thermal expansion.

The model for D_0^{M2} incorporates compositional terms from all three sites in clinopyroxene, and temperature. The positive effect of tetrahedral R^{3+} on D_0^{M2} is the largest contribution to the model, which is consistent with published studies (see above). The relationship between clinopyroxene compositional terms on the $^{VI}M1$ and $^{VIII}M2$ sites and D_0 are indirect and are tied to the solubility of the mineral in the melt (Wood & Blundy, 2003), which in turn is tied to the physico-chemical conditions of the system (largely melt composition). The model for D_0^{M2} is less robust that that for r_0^{M2}, largely because there are melt compositional effects that are not recorded in the composition of the clinopyroxene. We tested the Mg# and XH_2O of the melt, neither of which are significant predictors for D_0^{M2} (95% confidence interval).

The model for E^{M2} is less well constrained than for the other two $^{VIII}M2$ lattice-strain parameters,

suggesting that $^{VIII}M2$ site stiffness is not tied strongly to clinopyroxene composition, temperature or pressure. Despite a significantly lower predictive power, this model still has physical grounding. Stiffness of the $^{VIII}M2$ site is positively correlated with pressure, as might be expected following a simple Hooke's law relationship, and there are some subtle compositional controls imparted by the ^{IV}T and $^{VI}M1$ sites. The poor correlation between E^{M2}, clinopyroxene composition, temperature and pressure is also evident in published element partitioning models, where E^{M2} is either poorly predicted (Fig. 12c), or set to a fixed value (e.g. Dygert et al., 2014).

Diagrams of measured vs predicted D values for R^{3+} cations are given in Fig. 13a, showing the predictive power of the models over a compositional range between basalt and peralkaline phonolite. For the $^{VIII}M2$ site, 95% of the measured R^{3+} partition coefficients are reproduced within a factor of $^{+2.5}_{-2.9}$ (hard dashed lines), and in extreme cases, the model still reproduces D values within an order of magnitude, sufficient for the prediction of element partitioning trends over a wide range of $P-T-X$. D_{MREE}, including Sm, are reproduced more faithfully than D_{LREE}, because their radius is closer to r_0^{M2} (Fig. 13c, d), and, therefore, prediction of their partitioning behaviour is affected less strongly by inaccuracies in predicted E^{M2} values.

The clinopyroxene M1 site

Using a methodology similar to the $^{VIII}M2$ site, we fitted a predictive model for partitioning of R^{3+} cations onto the smaller $^{VI}M1$ site of clinopyroxene. Lattice-strain parabola were constrained by partitioning data for Cr, Ga, Sc, and, where suitable, the HREE Tm, Yb and Lu (Our IHPV experiments plus Hill et al., 2000; Fedele et al., 2009; Mollo et al., 2013; Dygert et al., 2014). The data set for the $^{VI}M1$ site partitioning model is small relative to that for the $^{VIII}M2$ site (n = 18), and because it is strongly skewed towards alkaline compositions, it has lower predictive power and is not recommended for application to mafic magmatic systems. Equations for the $^{VI}M1$ site lattice-strain parameters, as generated by multiple linear least squares regression, are given below and shown in Fig. 12 where b_i are the regression coefficients (Table 5) for the respective variables:

$$r_0^{M1} = b_{10} + b_{11}P + b_{12}X_{Mg}^{M2} + b_{13}X_{Fe^{3+}}^{M1} + b_{14}X_{Ca}^{M2} \tag{9}$$

$$lnD_0^{M1} = b_1 + b_2X_{Al}^{T} + b_3X_{Fe^{3+}}^{M1} + b_4X_{Ca}^{M2} + b_5X_{Na}^{M2} \tag{10}$$

$$E^{M1} = b_6 + b_7T + b_8P + b_9X_{Mg}^{M1} \tag{11}$$

The model for r_0^{M1} is robust and accurately reproduces the input data set. A negative pressure term may reflect compressional strain on the crystal lattice. Fe^{3+} cations have a positive effect on the size of the $^{VI}M1$ site, while E^{M1} is predicted more accurately than E^{M2} and is largely described by variations in temperature and pressure. Much like the $^{VIII}M2$ site, the stiffness of
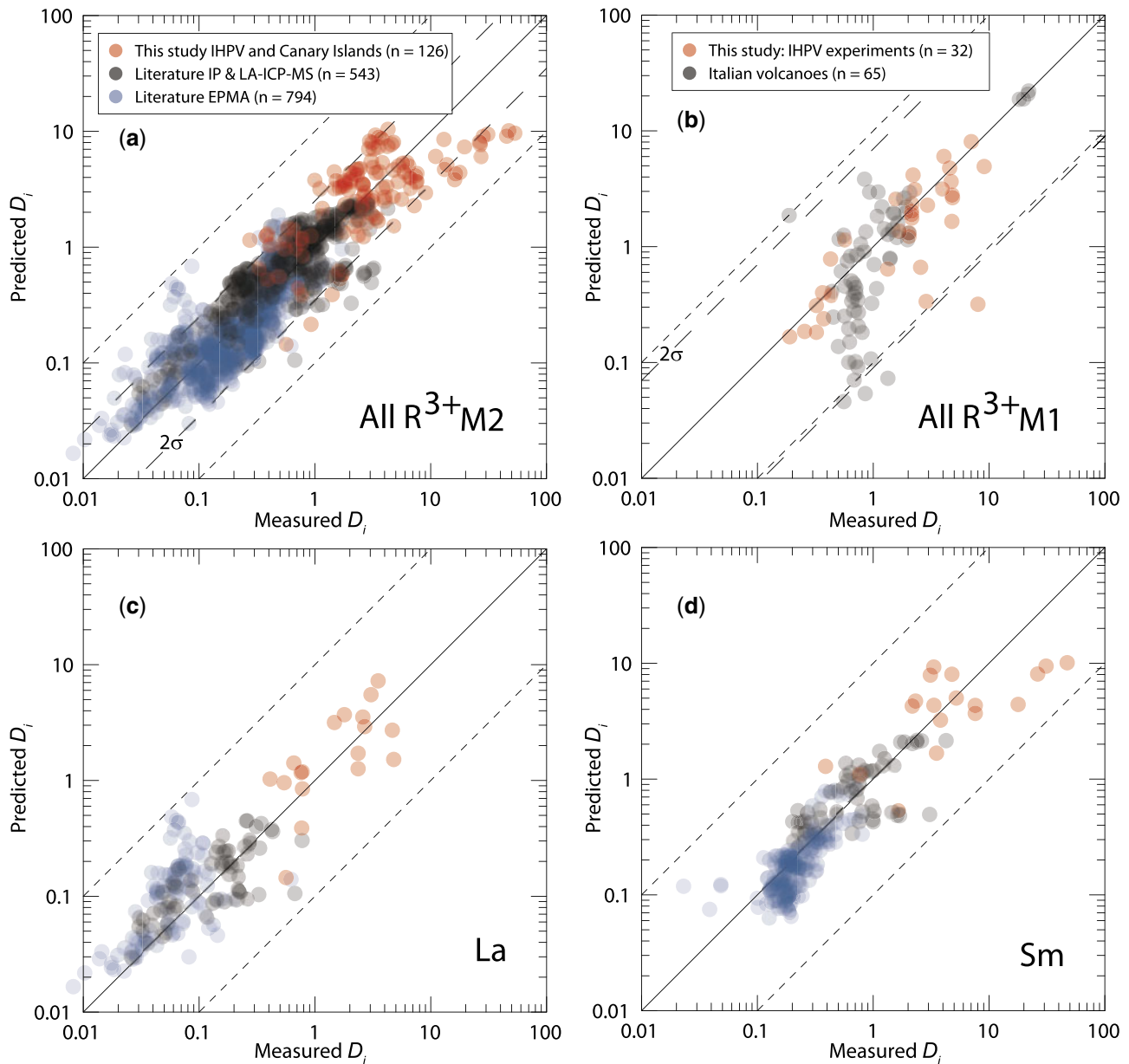
Fig. 13. Measured clinopyroxene–silicate melt partition-coefficients for 3+ cations vs those predicted by our empirical model. (a) shows a comparison between measured partition coefficients and model-derived values for the ^{VIII}M2 site of clinopyroxene. Hard dashed lines represent 95% (2σ) confidence intervals of the model, and correspond to maximum uncertainties of factor $^{+2.5}_{-2.9}$. Fine dashed lines represent 1 order of magnitude uncertainty (extreme outliers for ^{VIII}M2 model). Partition coefficients in this diagram are the REE La to Er for our IHPV experiments, Canary Islands rocks, and literature data from the Italian volcanoes (Wood & Trigila, 2001; Fedele *et al.*, 2009; Mollo *et al.*, 2013, 2016), and all the REE plus Y for the rest of the data compilation (Bédard, 2014), which is split by analytical methodology. (b) shows performance of the predictive model for the ^{VI}M1 site that is calibrated for alkaline magmatic systems, and includes data from our IHPV experiments and the Italian volcanoes (Fedele *et al.*, 2009; Mollo *et al.*, 2013, 2016). Maximum uncertainties at the 95% (2σ) confidence interval are a factor of $^{+7}_{-11}$, higher than for the ^{VIII}M2 site because of the smaller calibrating data set. (c) performance of the ^{VIII}M2 site model for La, and (d) for Sm.

the ^{VI}M1 site appears to be controlled dominantly by physico-chemical factors that are not recorded in the composition of the clinopyroxene.

The model for D_0^{M1} contains compositional terms from all three crystallographic sites in clinopyroxene. X_{Al}^T has a strong positive correlation with D_0^{M1}, consistent with a charge compensation mechanism that aids incorporation of R^{3+} cations, while terms for ^{VI}M1 and

^{VIII}M2 site cations may be indirectly recording melt compositional effects. Because D_0^{M1} is unusually high for our high-aegirine experiments, these had to be excluded from the fitting procedure to permit model convergence. Therefore, while the models for r_0^{M1} and E^{M1} are calibrated for use all the way to end-member aegirine, the model for the D_0^{M1} term is only calibrated for use up to ~Aeg$_{50}$. Further experiments at conditions
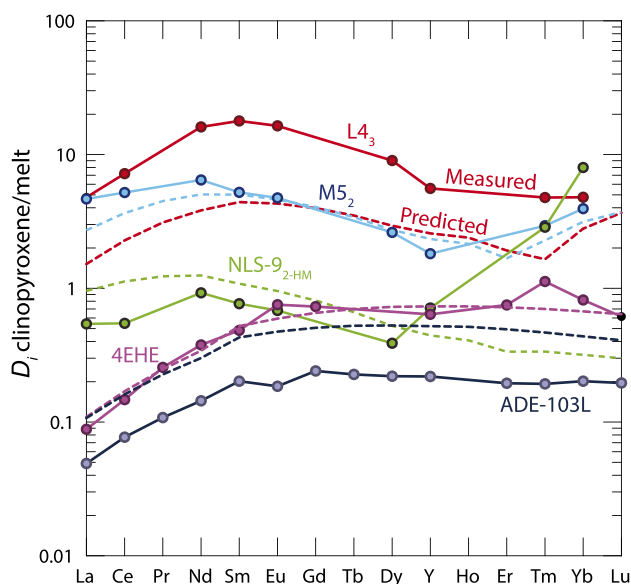
Fig. 14. Diagram showing measured and predicted element partition coefficients for REE^{3+}. The model does not introduce notable radius-dependent biases, except for in our high-aegirine clinopyroxene (NLS-9$_{2-HM}$ in green) for which D_{HREE} are strongly underpredicted, owing to inaccurate return of D_0^{M1}. Shown for comparison are two diopside–melt pairs: 4EHE from Hill *et al.* (2000), grown from a synthetic (NCMAS) basaltic andesite composition and ADE-103L from Lofgren *et al.* (2006) grown from a picritic composition based on the Angra dos Reis meteorite.
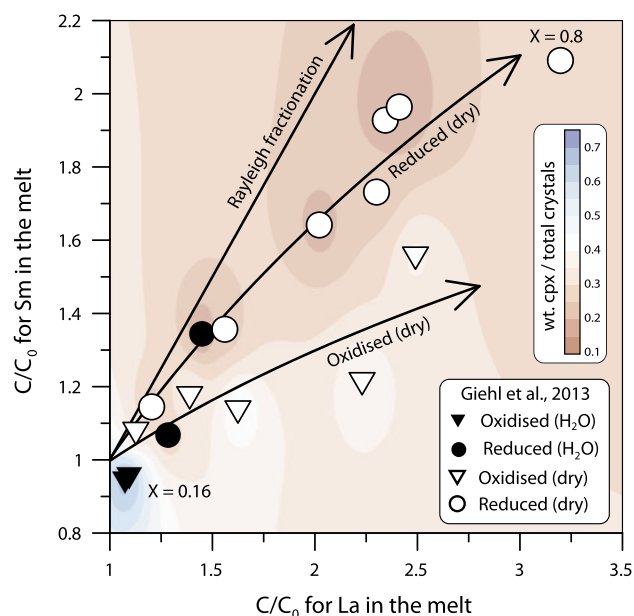

Fig. 15. Diagram showing model enrichment paths for La and Sm in residual melts during fractional crystallization of a peralkaline melt (MiKa dyke, Gardar Province, Greenland, see Marks & Markl, 2003). C/C_0 is the modelled concentration of La or Sm divided by the initial concentration of this element in the melt. Phase relations and clinopyroxene compositions were determined experimentally by Giehl *et al.* (2013) and pertain to both oxidising and reducing conditions (log $fO_2 = \Delta FMQ +1$ and -3), nominally dry to water bearing (to 3 wt % H_2O at 100 MPa). Colour shading indicates the weight fraction of clinopyroxene within the crystallizing assemblage. Bold arrows indicate residual enrichment pathways for the REE in the melt for Rayleigh fractionation (no incorporation into crystals), reduced dry conditions, and oxidised dry conditions (the latter two are least-squares power law fits to the data). For simplicity, this model does not consider REE incorporation into magnetite, alkali-feldspar, olivine, nepheline or aenigmatite (see Larsen, 1979; Kovalenko *et al.*, 1988; Mahood & Stimac, 1990; Fedele *et al.*, 2015), all of which are phases generated in the experiments of Giehl *et al.* (2013). Calculations follow White (2013).

between those that generated our medium and high-aegirine clinopyroxene would be required to better constrain the clinopyroxene compositional record of D_0^{M1} in strongly peralkaline Fe-rich magmas.

When applied to our experimental data, and the compilation of partition coefficients from Italian volcanoes (Fedele *et al.*, 2009; Mollo *et al.*, 2013, 2016), the $^{VI}M1$ stepwise model reproduces element partitioning data to a factor of $^{+7}_{-11}$ at the 95% confidence interval (Fig. 13b). Full regression reports are provided in Supplementary Data Electronic Appendix 5.

To assess the utility of the partitioning models and to monitor for potential introduction of radius-dependent bias, we show predicted REE patterns normalised to measured ratios for some literature data and our internally heated pressure vessel experiments (Fig. 14). The model accurately reproduces inter-element variations for the REE for all compositions, except for HREE on the $^{VI}M1$ site of clinopyroxene at aegirine contents exceeding ~50 mol % (NLS experiments) for which D_{HREE} are strongly under-predicted, owing to inaccurate return of D_0^{M1}. Positive or negative bias in absolute D_{REE} values occurs because of uncertainties in the modelled D_0^{M1} and D_0^{M2} parameters. For convenience, we provide an EXCEL spreadsheet for calculation of clinopyroxene–melt element partition coefficients for any trace element of 3+ valence that is large enough to fit onto the $^{VI}M1$ or $^{VIII}M2$ sites of clinopyroxene (Supplementary Data Electronic Appendix 6).

Implications for formation of REE deposits in evolved alkaline intrusions

The solubility of REE and HFSE minerals is strongly enhanced in peralkaline melts (Watson, 1979; Linnen & Keppler, 1997; Boehnke *et al.*, 2013; Aseri *et al.*, 2015), and thus the high concentration of these elements in peralkaline systems may (partially) reflect this fact (Dostal, 2017). Melts containing high concentrations of REE and HFSE are thought to be generated through low degrees of partial melting in the mantle, followed by residual enrichment during protracted fractional crystallization (Marks & Markl, 2017). The budget of REE and HFSE in a fractionating magma is influenced by the mineralogy of the crystallizing assemblage, and the extent to which these elements are incorporated at minor or trace concentrations.

Clinopyroxene is a major ferromagnesian phase that is commonly saturated throughout the entire differentiation histories of peralkaline magmatic systems (Ablay *et al.*, 1998; Marks & Markl, 2001; Möller & Williams-Jones, 2016). The composition of the fractionating

clinopyroxene has a strong impact on the absolute REE concentrations and REE pattern of the residual melt, and ultimately on the ability of a system to develop economic concentrations of the REE (e.g. Kogarko, 1990; Sørensen, 1992; Marks et al., 2011). Clinopyroxene in alkaline magmatic systems is initially calcic for mafic melts, and becomes increasingly sodic as crystal fractionation proceeds (Marks et al., 2004). Although the REE are compatible in the majority of our experimentally generated clinopyroxene, those approaching aegirine end-member composition, as found in evolved alkaline magmatic systems, have the lowest D_{REE} values (Fig. 6). Strongly alkaline magmatic systems are thought to crystallize abundant Ca-clinopyroxene early in their evolution that may deplete residual liquids with respect to REE. Consequently, even though crystallization of Na-clinopyroxene could enrich residual liquids with REE, the resultant concentration of these metals in the melt would remain low. However, clinopyroxene is not the only phase to crystallize from alkaline magmas, and the majority of additional silicate phases, such as olivine, biotite and feldspar have DREE $\ll$ 1, typically 1–4 orders of magnitude lower than clinopyroxene (Larsen, 1979; Kovalenko et al., 1988; Mahood & Stimac, 1990; Fedele et al., 2015). Consequently, if the mode of clinopyroxene is low enough, the bulk D_{REE} of the crystallizing assemblage would remain below unity, allowing the REE to become enriched in the residual silicate melt.

To give insight into the optimum conditions for residual magmatic enrichment of the REE in (per)alkaline systems we forward modelled the evolution of REE concentrations in the melt during fractional crystallization of a nepheline syenite body (Fig. 15; Supplementary Data Electronic Appendix 8). Phase relation data and clinopyroxene compositions are from the experimental study of Giehl et al. (2013). Their starting composition, based on the MiKa dyke, from the Gardar Province, Greenland, is already extremely evolved, with Mg# = 2, (Na + K)/Al = 1·44 and FeO* = 12 wt %. In these models, crystallization under water-bearing, oxidising conditions produces a high fraction of clinopyroxene that depletes residual melts with respect to Sm, while subtly enriching La. Dry conditions promote abundant alkali feldspar (Afs) crystallization, which effectively enriches the REE content of residual melts. Under oxidising, dry conditions, the La/Sm ratio of the residual melt increases with fractionation, because Sm is more effectively incorporated into clinopyroxene. Residual enrichment is most effective under dry, reducing conditions because of a relatively lower fraction of clinopyroxene within the crystallizing assemblage. Because of this, the REE enrichment path of the residual melt is close to that of ideal Rayleigh fractionation. Under these reducing, dry conditions and at a temperature of 750°C, the experiments of Giehl et al. (2013) attained a crystal fraction of 0·8. Here, residual melts would have 3·2 times the La concentration and 2 times the Sm concentration relative to their starting composition (C/C_0). Clinopyroxene generated in the higher fO_2 experiments

of Giehl et al., (2013) did not display systematic increases to $^{VI}Fe^{3+}$ and ^{IV}Al, nor higher modelled D_0^{M1} and D_0^{M2} values relative to their reduced experimental clinopyroxene (Supplementary Data Electronic Appendix 8). The enhanced residual enrichment of the REE under reduced conditions here reflect lower proportions of clinopyroxene in the crystallizing assemblage, rather than a clinopyroxene compositional control.

Considering the modelling results above alongside our experimental and Canary Islands data, the best systems to develop high REE concentrations are those that would produce small proportions of Ca-clinopyroxene early in their crystallization histories, quickly evolving to more sodic compositions that crystallize aegirine clinopyroxene. Cooling under low-pressure, dry, reducing conditions produces abundant alkali feldspar that in the case of a peralkaline composition, would serve to further increase the alkalinity of the residual melt. Low-degrees of source melting would produce primary melts with (1) high REE concentrations and (2) low melt Mg + Fe, and low modal abundance of clinopyroxene, which would aid residual enrichment in silicate melt via fractional crystallization.

The HREE-rich nature of peralkaline silicate magmatic systems, both granites and nepheline syenites, is compatible with fractionation of moderately sodic clinopyroxene that has high D_{LREE}/D_{HREE} (e.g. Möller & Williams-Jones, 2016; Dostal, 2017). As crystal fractionation progresses and clinopyroxene composition evolves toward the aegirine end-member composition, D_{LREE}/D_{HREE} decreases (Fig. 6). This systematic change in element partitioning behaviour would result in strong HREE enrichment in aegirine-clinopyroxene cumulates, and would enrich the residual melt with respect to LREE-MREE.

CONCLUSIONS

Eleven IHPV crystallization experiments and six natural clinopyroxene–glass pairs from Tenerife, Canary Islands were investigated to determine the clinopyroxene–melt partitioning behaviour of trace elements in sodic alkali-rich magmas and to extend empirical partitioning models toward the aegirine end-member clinopyroxene composition. Our experiments reveal three distinct element partitioning behaviours for Na-rich clinopyroxene that depend on the aegirine content of clinopyroxene. Each of these is associated with a distinct major element exchange vector and it is unclear at present if the transition between these behaviours is smooth or step-like. For all investigated compositions, apparent REE partition coefficients are correlated with the ^{IV}Al content of clinopyroxene, confirming that a REE incorporation mechanism coupled with ^{IV}Al-Si substitution extends to peralkaline conditions. $HFSE^{4+}$ and $HFSE^{5+}$ partition coefficients determined from low-aegirine experiments (Aeg$_{5-25}$) and Canary Islands pyroclasts are also correlated with the ^{IV}Al content of

clinopyroxene. No such correlation was found at aegirine contents exceeding Aeg_{26}, indicating a distinct incorporation mechanism for HFSE in alkali-rich systems that is correlated with the ^{VIII}Na content of clinopyroxene.

Fits of R^{3+} partition-coefficients to the lattice-strain model of Blundy & Wood (1994) indicate expansion of the $^{VIII}M2$ site with increasing Na^+_{M2}, to a maximum $r^{3+}_{0,M2}$ of $1\cdot12\,\text{Å}$ at $Na^+_{M2} = 0\cdot4$ c.p.f.u. Further expansion did not occur at higher Na contents, rather both the $^{VI}M1$ and $^{VIII}M2$ sites of clinopyroxene shrink in response to increasing $\sum R^{3+}_{M1}$. Charge effects lead to a progressive increase in D^{M1}_0 at the expense of D^{M2}_0, following the exchanges $^{VIII}Ca^{2+}$ for Na^+ and $^{VI}M^{2+}$ for Fe^{3+}.

We have calibrated a new empirical model that predicts partition coefficients for R^{3+} ions between silicate melt and the $^{VI}M1$ and $^{VIII}M2$ sites of clinopyroxene. This model requires as input clinopyroxene major element composition, temperature and pressure and is calibrated for use on compositions between tholeiitic basalt and peralkaline phonolite. For convenience we provide an EXCEL spreadsheet of this model (Supplementary Data Electronic Appendix 6). Application of our empirical partitioning model to a peralkaline-silicate composition from the Gardar Province, Greenland, indicates that fractional crystallization under dry, low-pressure, low-fO_2 conditions permits efficient orthomagmatic enrichment of the REE. Under these conditions abundant Ca-Mg rich clinopyroxene crystallization is supressed in favour of an alkalifeldspar dominated assemblage with lower bulk D_{REE} values. Here, clinopyroxene mode represents the dominant control on the REE budget of the residual melt, whereas clinopyroxene composition determines its REE pattern. The modelling further suggests that nepheline syenites which host REE deposits originate from lowdegree melts with sufficient alkali enrichment to saturate clinopyroxene similar to our medium-aegirine clinopyroxene (Aeg_{25-50}). Fractionation of such clinopyroxene enriches residual melts with respect to the HREE, in accord with the composition of REE-mineralised nepheline syenite systems.

ACKNOWLEDGEMENTS

FUNDING

SUPPLEMENTARY DATA

Supplementary data are available at *Journal of Petrology* online.

REFERENCES

Ablay, G. J., Carroll, M. R., Palmer, M. R., Martí, J. & Sparks, R. S. J. (1998). Basanite–phonolite lineages of the Teide–Pico Viejo volcanic complex, Tenerife, Canary Islands. *Journal of Petrology* **39**, 905–936.

Ablay, G. J., Ernst, G. G. J., Marti, J. & Sparks, R. S. J. (1995). The ~2 ka subplinian eruption of Montaña Blanca, Tenerife. *Bulletin of Volcanology* **57**, 337–355.

Adam, J. & Green, T. (2006). Trace element partitioning between mica- and amphibole-bearing garnet lherzolite and hydrous basanitic melt: 1. Experimental results and the investigation of controls on partitioning behaviour. *Contributions to Mineralogy and Petrology* **152**, 1–17.

Adam, J., Green, T. H. & Sie, S. H. (1993). Proton microprobe determined partitioning of Rb, Sr, Ba, Y, Zr, Nb and Ta between experimentally produced amphiboles and silicate melts with variable F content. *Chemical Geology* **109**, 29–49.

Akasaka, M. & Onuma, K. (1980). The join CaMgSi2O6-CaFe AlSiO6-CaTiAl2O6 and its bearing on the Ti-rich fassaitic pyroxenes. *Contributions to Mineralogy and Petrology* **71**, 301–312.

Albert, H., Costa, F. & Martí, J. (2015). Timing of magmatic processes and unrest associated with mafic historical monogenetic eruptions in Tenerife Island. *Journal of Petrology* **56**, 1945–1966.

Andújar, J. & Scaillet, B. (2012). Experimental constraints on parameters controlling the difference in the eruptive dynamics of phonolitic magmas: the case of Tenerife (Canary Islands). *Journal of Petrology* **53**, 1777–1806.

Aseri, A. A., Linnen, R. L., Che, X. D., Thibault, Y. & Holtz, F. (2015). Effects of fluorine on the solubilities of Nb, Ta, Zr and Hf minerals in highly fluxed water-saturated haplogranitic melts. *Ore Geology Reviews* **64**, 736–746.

Bédard, J. H. (2014). Parameterizations of calcic clinopyroxene—Melt trace element partition coefficients. *Geochemistry, Geophysics, Geosystems* **15**, 303–336.

Berndt, J., Liebske, C., Holtz, F., Freise, M., Nowak, M., Ziegenbein, D., Hurkuck, W. & Koepke, J. (2002). A combined rapid-quench and H_2-membrane setup for internally heated pressure vessels: description and application for water solubility in basaltic melts. *American Mineralogist* **87**, 1717–1726.

Blundy, J. & Dalton, J. (2000). Experimental comparison of trace element partitioning between clinopyroxene and melt in carbonate and silicate systems, and implications for mantle metasomatism. *Contributions to Mineralogy and Petrology* **139**, 356–371.

Blundy, J. & Wood, B. (1994). Prediction of crystal–melt partition coefficients from elastic moduli. *Nature* **372**, 452–454.

Blundy, J. D., Robinson, J. A. C. & Wood, B. J. (1998). Heavy REE are compatible in clinopyroxene on the spinel lherzolite solidus. *Earth and Planetary Science Letters* **160**, 493–504.

Boehnke, P., Watson, E. B., Trail, D., Harrison, T. M. & Schmitt, A. K. (2013). Zircon saturation re-revisited. *Chemical Geology* **351**, 324–334.

Borchert, M., Wilke, M., Schmidt, C., Cauzid, J. & Tucoulou, R. (2010). Partitioning of Ba, La, Yb and Y between haplogranitic melts and aqueous solutions: an experimental study. *Chemical Geology* **276**, 225–240.

Borst, A. M. A. M., Friis, H., Nielsen, T. F. D. & Waight, T. E. (2018). Bulk and mush melt evolution in agpaitic intrusions: insights from compositional zoning in eudialyte, Ilímaussaq complex, South Greenland. *Journal of Petrology* **59**, 589–612.

Boudreau, A. E. (2004). PALLADIUM, a program to model the chromatographic separation of the platinum-group elements, base metals and sulfur in a solidifying pile of igneous crystals. *The Canadian Mineralogist* **42**, 393–403.

Brown, R. J., Barry, T. L., Branney, M. J., Pringle, M. S. & Bryan, S. E. (2003). The Quaternary pyroclastic succession of southeast Tenerife, Canary Islands: explosive eruptions, related caldera subsidence, and sector collapse. *Geological Magazine* **140**, 265–288.

Bryan, S. E., Martí, J. & Cas, R. A. F. (1998). Stratigraphy of the Bandas del Sur Formation: an extracaldera record of Quaternary phonolitic explosive eruptions from the Las Cañadas edifice, Tenerife (Canary Islands). *Geological Magazine* **135**, 605–636.

Carracedo, J. C., Badiola, E. R., Guillou, H., Paterne, M., Scaillet, S., Torrado, F. J. P., Paris, R., Fra-Paleo, U. & Hansen, A. (2007). Eruptive and structural history of Teide Volcano and rift zones of Tenerife, Canary Islands. *Geological Society of America Bulletin* **119**, 1027–1051.

Carroll, M. R. & Blank, J. G. (1997). The solubility of H_2O in phonolitic melts. *American Mineralogist* **82**, 549–556.

Cherniak, D. J. & Dimanov, A. (2010). Diffusion in pyroxene, mica and amphibole. *Reviews in Mineralogy and Geochemistry* **72**, 641–690.

Chou, I.-M. (1986). Permeability of precious metals to hydrogen at 2 kb total pressure and elevated temperatures. *American Journal of Science* **286**, 638–658.

Corgne, A. & Wood, B. J. (2005). Trace element partitioning and substitution mechanisms in calcium perovskites. *Contributions to Mineralogy and Petrology* **149**, 85–97.

Coumans, J. P., Stix, J., Clague, D. A., Minarik, W. G. & Layne, G. D. (2016). Melt-rock interaction near the Moho: evidence from crystal cargo in lavas from near-ridge seamounts. *Geochimica et Cosmochimica Acta* **191**, 139–164.

Dare, S. A. S., Barnes, S.-J., Beaudoin, G., Méric, J., Boutroy, E. & Potvin-Doucet, C. (2014). Trace elements in magnetite as petrogenetic indicators. *Mineralium Deposita* **49**, 785–796.

Deer, W. A., Howie, R. A. & Zussman, J. (1992). *An Introduction to the Rock-Forming Minerals*. New York: Longman Group Ltd.

Dostal, J. (2017). Rare earth element deposits of alkaline igneous rocks. *Resources* **6**, 34–12.

Downes, H., Balaganskaya, E., Beard, A., Liferovich, R. & Demaiffe, D. (2005). Petrogenetic processes in the ultramafic, alkaline and carbonatitic magmatism in the Kola Alkaline Province: a review. *Lithos* **85**, 48–75.

Droop, G. T. R. (1987). A general equation for estimating Fe^{3+} concentrations in ferromagnesian silicates and oxides from microprobe analyses, using stoichiometric criteria. *Mineralogical Magazine* **51**, 431–435.

Dygert, N., Liang, Y., Sun, C. & Hess, P. (2014). An experimental study of trace element partitioning between augite and Fe-rich basalts. *Geochimica et Cosmochimica Acta* **132**, 170–186.

Edgar, C. J., Wolff, J. A., Olin, P. H., Nichols, H. J., Pittari, A., Cas, R. A. F., Reiners, P. W., Spell, T. L. & Martí, J. (2007). The late Quaternary Diego Hernandez Formation, Tenerife: volcanology of a complex cycle of voluminous explosive phonolitic eruptions. *Journal of Volcanology and Geothermal Research* **160**, 59–85.

Eugster, H. P. & Wones, D. R. (1962). Stability relations of the ferruginous biotite, annite. *Journal of Petrology* **3**, 82–125.

Fedele, L., Lustrino, M., Melluso, L., Morra, V., Zanetti, A. & Vannucci, R. (2015). Trace-element partitioning between plagioclase, alkali feldspar, Ti-magnetite, biotite, apatite, and evolved potassic liquids from Campi Flegrei (Southern Italy). *American Mineralogist* **100**, 233–249.

Fedele, L., Zanetti, A., Morra, V., Lustrino, M., Melluso, L. & Vannucci, R. (2009). Clinopyroxene/liquid trace element partitioning in natural trachyte–trachyphonolite systems: insights from Campi Flegrei (southern Italy). *Contributions to Mineralogy and Petrology* **158**, 337–356.

Flower, M. F. J. (1974). Phase relations of titan-acmite in the system sodium oxide-iron (III) oxide-aluminum oxide-titanium dioxide-silicon dioxide at 1000 bars total water pressure. *American Mineralogist* **59**, 536–548.

Foley, S. F., Prelevic, D., Rehfeldt, T. & Jacob, D. E. (2013). Minor and trace elements in olivines as probes into early igneous and mantle melting processes. *Earth and Planetary Science Letters* **363**, 181–191.

Francis, D. & Minarik, W. (2008). Aluminum-dependent trace element partitioning in clinopyroxene. *Contributions to Mineralogy and Petrology* **156**, 439–451.

Gaetani, G. A. (2004). The influence of melt structure on trace element partitioning near the peridotite solidus. *Contributions to Mineralogy and Petrology* **147**, 511–527.

Gaetani, G. A. & Grove, T. L. (1995). Partitioning of rare earth elements between clinopyroxene and silicate melt: crystal-chemical controls. *Geochimica et Cosmochimica Acta* **59**, 1951–1962.

Gaillard, F., Scaillet, B. & Pichavant, M. (2002). Kinetics of iron oxidation-reduction in hydrous silicic melts. *American Mineralogist* **87**, 829–837.

Giehl, C., Marks, M. & Nowak, M. (2013). Phase relations and liquid lines of descent of an iron-rich peralkaline phonolitic melt: an experimental study. *Contributions to Mineralogy and Petrology* **165**, 283–304.

Giordano, D., Nichols, A. R. L. & Dingwell, D. B. (2005). Glass transition temperatures of natural hydrous melts: a relationship with shear viscosity and implications for the welding process. *Journal of Volcanology and Geothermal Research* **142**, 105–118.

Girnis, A. V., Bulatov, V. K., Brey, G. P., Gerdes, A. & Höfer, H. E. (2013). Trace element partitioning between mantle minerals and silico-carbonate melts at 6–12 GPa and applications to mantle metasomatism and kimberlite genesis. *Lithos* **160–161**, 183–200.

Goodenough, K. M., Schilling, J., Jonsson, E., Kalvig, P., Charles, N., Tuduri, J., Deady, E. A., Sadeghi, M., Schiellerup, H., Müller, A., Bertrand, G., Arvanitidis, N., Eliopoulos, D. G., Shaw, R. A., Thrane, K. & Keulen, N. (2016). Europe's rare earth element resource potential: an overview of REE metallogenetic provinces and their geodynamic setting. *Ore Geology Reviews* **72**, 838–856.

Guillou, H., Carracedo, J. C., Paris, R. & Pérèz Torrado, F. J. (2004). Implications for the early shield-stage evolution of Tenerife from K/Ar ages and magnetic stratigraphy. *Earth and Planetary Science Letters* **222**, 599–614.

Gurenko, A. A., Hoernle, K. A., Hauff, F., Schmincke, H.-U., Han, D., Miura, Y. N. & Kaneoka, I. (2006). Major, trace element and Nd–Sr–Pb–O–He–Ar isotope signatures of shield stage lavas from the central and western Canary Islands: insights into mantle and crustal processes. *Chemical Geology* **233**, 75–112.

Hanchar, J. M., Finch, R. J., Hoskin, P. W. O., Watson, E. B., Cherniak, D. J. & Mariano, A. N. (2001). Rare earth elements in synthetic zircon: part 1. Synthesis, and rare earth element and phosphorus doping. *American Mineralogist* **86**, 667–680.

Hazen, R. M. & Finger, L. W. (1979). Bulk modulus-volume relationship for cation-anion polyhedra. *Journal of Geophysical Research: Solid Earth* **84**, 6723–6728.

Hill, E., Blundy, J. D. & Wood, B. J. (2011). Clinopyroxene-melt trace element partitioning and the development of a predictive model for HFSE and Sc. *Contributions to Mineralogy and Petrology* **161**, 423–438.

Hill, E., Wood, B. J. & Blundy, J. D. (2000). The effect of Ca-Tschermaks component on trace element partitioning between clinopyroxene and silicate melt. *Lithos* **53**, 203–215.

Huang, F., Lundstrom, C. C. & McDonough, W. F. (2006). Effect of melt structure on trace-element partitioning between clinopyroxene and silicic, alkaline, aluminous melts. *American Mineralogist* **91**, 1385–1400.

Jugo, P. J., Wilke, M. & Botcharnikov, R. E. (2010). Sulfur K-edge XANES analysis of natural and synthetic basaltic glasses: implications for S speciation and S content as function of oxygen fugacity. *Geochimica et Cosmochimica Acta* **74**, 5926–5938.

Kennedy, A. K., Lofgren, G. E. & Wasserburg, G. J. (1993). An experimental study of trace element partitioning between olivine, orthopyroxene and melt in chondrules: equilibrium values and kinetic effects. *Earth and Planetary Science Letters* **115**, 177–195.

Kogarko, L. N. (1990). Ore-forming potential of alkaline magmas. *Lithos* **26**, 167–175.

Kovalenko, V. I., Hervig, R. L. & Sheridan, M. F. (1988). Ion microprobe analyses of trace elements in anorthoclase, hedenbergite, aenigmatite, quartz, apatite and glass in pantellerite: evidence for high water contents in pantellerite melt. *American Mineralogist* **73**, 1038–1045.

Kress, V. C. & Carmichael, I. S. E. (1991). The compressibility of silicate liquids containing Fe2O3 and the effect of composition, temperature, oxygen fugacity and pressure on their redox states. *Contributions to Mineralogy and Petrology* **108**, 82–92.

Kumazawa, M. (1969). The elastic constants of single-crystal orthopyroxene. *Journal of Geophysical Research* **74**, 5973–5980.

Larsen, L. M. (1979). Distribution of REE and other trace elements between phenocrysts and peralkaline undersaturated magmas, exemplified by rocks from the Gardar igneous province, South Greenland. *Lithos* **12**, 303–315.

Law, K. M., Blundy, J. D., Wood, B. J. & Ragnarsdottir, K. V. (2000). Trace element partitioning between wollastonite and silicate-carbonate melt. *Mineralogical Magazine* **64**, 651–661.

Linnen, R. L. & Keppler, H. (1997). Columbite solubility in granitic melts: consequences for the enrichment and fractionation of Nb and Ta in the Earth's crust. *Contributions to Mineralogy and Petrology* **128**, 213–227.

Lofgren, G. E., Huss, G. R. & Wasserburg, G. J. (2006). An experimental study of trace-element partitioning between Ti-Al-clinopyroxene and melt: equilibrium and kinetic effects including sector zoning. *American Mineralogist* **91**, 1596–1606.

Lundstrom, C. C., Shaw, H. F., Ryerson, F. J., Phinney, D. L., Gill, J. B. & Williams, Q. (1994). Compositional controls on the partitioning of U, Th, Ba, Pb, Sr and Zr between clinopyroxene and haplobasaltic melts: implications for uranium series disequilibria in basalts. *Earth and Planetary Science Letters* **128**, 407–423.

Mahood, G. A. & Stimac, J. A. (1990). Trace-element partitioning in pantellerites and trachytes. *Geochimica et Cosmochimica Acta* **54**, 2257–2276.

Marks, M., Halama, R., Wenzel, T. & Markl, G. (2004). Trace element variations in clinopyroxene and amphibole from alkaline to peralkaline syenites and granites: implications for mineral-melt trace-element partitioning. *Chemical Geology* **211**, 185–215.

Marks, M. & Markl, G. (2001). Fractionation and assimilation processes in the alkaline augite syenite unit of the Ilímaussaq intrusion, South Greenland, as deduced from phase equilibria. *Journal of Petrology* **42**, 1947–1969.

Marks, M. A. W., Hettmann, K., Schilling, J., Frost, B. R. & Markl, G. (2011). The mineralogical diversity of alkaline igneous rocks: critical factors for the transition from miaskitic to agpaitic phase assemblages. *Journal of Petrology* **52**, 439–455.

Marks, M. & Markl, G. (2003). Ilímaussaq 'En Miniature': closed-system fractionation in an agpaitic Dyke rock from the Gardar province, South Greenland (Contribution to the Mineralogy of Ilímaussaq No. 117). *Mineralogical Magazine* **67**, 893–919.

Marks, M. A. W. & Markl, G. (2017). A global review on agpaitic rocks. *Earth-Science Reviews* **173**, 229–258.

Morimoto, N. (1989). Nomenclature of pyroxenes. *Mineralogical Journal* **14**, 198–221.

Möller, V. & Williams-Jones, A. E. (2016). Petrogenesis of the Nechalacho layered suite, Canada: magmatic evolution of a REE-Nb-rich nepheline syenite intrusion. *Journal of Petrology* **57**, 229–276.

Mollo, S., Blundy, J. D., Giacomoni, P., Nazzari, M., Scarlato, P., Coltorti, M., Langone, A. & Andronico, D. (2017). Clinopyroxene-melt element partitioning during interaction between trachybasaltic magma and siliceous crust: clues from quartzite enclaves at Mt. Etna volcano. *Lithos* **284–285**, 447–461.

Mollo, S., Blundy, J. D., Iezzi, G., Scarlato, P. & Langone, A. (2013). The partitioning of trace elements between clinopyroxene and trachybasaltic melt during rapid cooling and crystal growth. *Contributions to Mineralogy and Petrology* **166**, 1633–1654.

Mollo, S., Blundy, J., Scarlato, P., De Cristofaro, S. P., Tecchiato, V., Di Stefano, F., Vetere, F., Holtz, F. & Bachmann, O. (2018). An integrated P-T-H2O-lattice strain model to quantify the role of clinopyroxene fractionation on REE+Y and HFSE patterns of mafic alkaline magmas: application to eruptions at Mt. Etna. *Earth-Science Reviews* **185**, 32–56. Elsevier

Mollo, S., Forni, F., Bachmann, O., Blundy, J. D., De Astis, G. & Scarlato, P. (2016). Trace element partitioning between clinopyroxene and trachy-phonolitic melts: a case study from the Campanian Ignimbrite (Campi Flegrei, Italy). _Lithos_ **252–253**, 160–172.

Mollo, S. & Vona, A. (2014). The geochemical evolution of clinopyroxene in the Roman Province: a window on decarbonation from wall-rocks to magma. _Lithos_ **192–195**, 1–7.

Moore, G., Vennemann, T. & Carmichael, I. S. E. (1998). An empirical model for the solubility of H_2O in magmas to 3 kilobars. _American Mineralogist_ **83**, 36–42.

Mungall, J. & Brenan, J. (2014). Partitioning of platinum-group elements and Au between sulfide liquid and basalt and the origins of mantle-crust fractionation of the chalcophile elements. _Geochimica et Cosmochimica Acta_ **125**, 265–289.

Mysen, B. O., Virgo, D. & Seifert, F. A. (1982). The structure of silicate melts: implications for chemical and physical properties of natural magma. _Reviews of Geophysics_ **20**, 353–383.

Mysen, B. O., Virgo, D. & Seifert, F. A. (1985). Relationships between properties and structure of aluminosilicate melts. _American Mineralogist_ **70**, 88–105.

Niu, Y. (2004). Bulk-rock major and trace element compositions of abyssal peridotites: implications for mantle melting, melt extraction and post-melting processes beneath Mid-Ocean ridges. _Journal of Petrology_ **45**, 2423–2458.

Olin, P. H. & Wolff, J. A. (2010). Rare earth and high field strength element partitioning between iron-rich clinopyroxenes and felsic liquids. _Contributions to Mineralogy and Petrology_ **160**, 761–775.

Onuma, N., Higuchi, H., Wakita, H. & Nagasawa, H. (1968). Trace element partition between two pyroxenes and the host lava. _Earth and Planetary Science Letters_ **5**, 47–51.

Paton, C., Hellstrom, J., Paul, B., Woodhead, J. & Hergt, J. (2011). Iolite: freeware for the visualisation and processing of mass spectrometric data. _Journal of Analytical Atomic Spectrometry_ **26**, 2508–2518.

Peters, S. T. M., Troll, V. R., Weis, F. A., Dallai, L., Chadwick, J. P. & Schulz, B. (2017). Amphibole megacrysts as a probe into the deep plumbing system of Merapi volcano, Central Java, Indonesia. _Contributions to Mineralogy and Petrology_ **172**, 1–20.

Putirka, K. D. (2008). Thermometers and barometers for volcanic systems. _Reviews in Mineralogy and Geochemistry_ **69**, 61–120.

Rasband, W. S. (2016). _ImageJ_. Bethesda, Maryland, USA: U.S. National Institutes of Health.

Redhammer, G. J., Amthauer, G., Roth, G., Tippelt, G. & Lottermoser, W. (2006). Single-crystal X-ray diffraction and temperature dependent 57Fe Mössbauer spectroscopy on the hedenbergite-aegirine (Ca,Na)(Fe^{2+},Fe^{3+})Si2O6 solid solution. _American Mineralogist_ **91**, 1271–1292.

Reguir, E. P., Chakhmouradian, A. R., Pisiak, L., Halden, N. M., Yang, P., Xu, C., Kynický, J. & Couëslan, C. G. (2012). Trace-element composition and zoning in clinopyroxene- and amphibole-group minerals: implications for element partitioning and evolution of carbonatites. _Lithos_ **128**, 27–45.

Schmidt, B. C. & Behrens, H. (2008). Water solubility in phonolite melts: influence of melt composition and temperature. _Chemical Geology_ **256**, 258–267.

Schmidt, M. W., Connolly, J. A. D., Günther, D. & Bogaerts, M. (2006). Element partitioning: the role of melt structure and composition. _Science_ **312**, 1646–1650.

Severs, M. J., Beard, J. S., Fedele, L., Hanchar, J. M., Mutchler, S. R. & Bodnar, R. J. (2009). Partitioning behavior of trace elements between dacitic melt and plagioclase, orthopyroxene, and clinopyroxene based on laser ablation ICPMS analysis of silicate melt inclusions. _Geochimica et Cosmochimica Acta_ Elsevier Ltd **73**, 2123–2141.

Shannon, R. D. (1976). Revised effective ionic radii and systematic studies of interatomic distances in halides and chalcogenides. _Acta Crystallographica Section A: Crystal Physics, Diffraction, Theoretical and General Crystallography_ **32**, 751–767.

Shearer, C. K. & Larsen, L. M. (1994). Sector-zoned aegirine from the Ilimaussaq alkaline intrusion, South Greenland; implications for trace-element behavior in pyroxene. _American Mineralogist_ **79**, 340–352.

Sjöqvist, A., Cornell, D., Andersen, T., Erambert, M., Ek, M. & Leijd, M. (2013). Three compositional varieties of rare-earth element ore: eudialyte-group minerals from the Norra Kärr alkaline complex, Southern Sweden. _Minerals_ **3**, 94–120.

Slack, J. F. & Trumbull, R. B. (2011). Tourmaline as a recorder of ore-forming processes. _Elements_ **7**, 321–326.

Sørensen, H. (1992). Agpaitic nepheline syenites: a potential source of rare elements. _Applied Geochemistry_ **7**, 417–427.

Spera, F. J. & Bohrson, W. A. (2001). Energy-constrained open-system magmatic processes I: general model and energy-constrained assimilation and fractional crystallization (EC-AFC) formulation. _Journal of Petrology_ **42**, 999–1018.

Stevens, J. (1996). _Applied Multivariate Analysis for the Social Sciences_. Mahwah, NJ: Lawrence Erlbaum.

Sun, C. & Liang, Y. (2012). Distribution of REE between clinopyroxene and basaltic melt along a mantle adiabat: effects of major element composition, water, and temperature. _Contributions to Mineralogy and Petrology_ **163**, 807–823.

Thirlwall, M. F., Singer, B. S. & Marriner, G. F. (2000). ^{39}Ar–^{40}Ar ages and geochemistry of the basaltic shield stage of Tenerife, Canary Islands, Spain. _Journal of Volcanology and Geothermal Research_ **103**, 247–297.

Troll, V. & Schmincke, H. (2002). Magma mixing and crustal recycling recorded in ternary feldspar from compositionally zoned peralkaline ignimbrite "A", Gran Canaria, Canary Islands. _Journal of Petrology_ **43**, 243–270.

van Hinsberg, V. J., Migdisov, A. A. & Williams-Jones, A. E. (2010). Reading the mineral record of fluid composition from element partitioning. _Geology_ **38**, 847–850.

Van Orman, J. A., Grove, T. L. & Shimizu, N. (2001). Rare earth element diffusion in diopside: influence of temperature, pressure, and ionic radius, and an elastic model for diffusion in silicates. _Contributions to Mineralogy and Petrology_ **141**, 687–703.

Vasyukova, O. V. & Williams-Jones, A. E. (2019). Tracing the evolution of a fertile REE granite by modelling amphibole-melt partitioning, the Strange Lake story. _Chemical Geology_ **514**, 79–89.

Watson, E. B. (1979). Zircon saturation in felsic liquids: experimental results and applications to trace element geochemistry. _Contributions to Mineralogy and Petrology_ **70**, 407–419.

Weidner, D. J. & Vaughan, M. T. (1982). Elasticity of pyroxenes: effects of composition versus crystal structure. _Journal of Geophysical Research_ **87**, 9349–9353.

Wiesmaier, S., Troll, V. R., Carracedo, J. C., Ellam, R. M., Bindeman, I. & Wolff, J. A. (2012). Bimodality of lavas in the Teide–Pico Viejo succession in Tenerife—The role of crustal melting in the origin of recent phonolites. _Journal of Petrology_ **53**, 2465–2495.

Wood, B. J. & Blundy, J. D. (1997). A predictive model for rare earth element partitioning between clinopyroxene and anhydrous silicate melt. _Contributions to Mineralogy and Petrology_ **129**, 166–181.

Wood, B. J. & Blundy, J. D. (2001). The effect of cation charge on crystal–melt partitioning of trace elements. _Earth and Planetary Science Letters_ **188**, 59–71.

Wood, B. J. & Blundy, J. D. (2003). Trace element partitioning under crustal and uppermost mantle conditions: the influences of ionic radius, cation charge, pressure, and temperature. In: Carlson, R. W. (ed.) *The Mantle and Core: Treatise on Geochemistry*. Elsevier, pp. 395–424.

Wood, B. J. & Blundy, J. D. (2014). Trace element partitioning: the influences of ionic radius, cation charge, pressure, and temperature. In: Carlson, R. W. (ed.) *The Mantle and Core: Treatise on Geochemistry*, 2nd edn. Elsevier, pp. 421–445.

Wood, B. J. & Trigila, R. (2001). Experimental determination of aluminous clinopyroxene–melt partition coefficients for potassic liquids, with application to the evolution of the Roman province potassic magmas. *Chemical Geology* **172**, 213–223.

Workman, R. K. & Hart, S. R. (2005). Major and trace element composition of the depleted MORB mantle (DMM). *Earth and Planetary Science Letters* **231**, 53–72.

Wörner, G., Beusen, J.-M., Duchateau, N., Gijbels, R. & Schmincke, H.-U. (1983). Trace element abundances and mineral/melt distribution coefficients in phonolites from the Laacher See volcano (Germany). *Contributions to Mineralogy and Petrology* **84**, 152–173.

Xu, C., Kynicky, J., Chakhmouradian, A. R., Campbell, I. H. & Allen, C. M. (2010). Trace-element modeling of the magmatic evolution of rare-earth-rich carbonatite from the Miaoya deposit, Central China. *Lithos* **118**, 145–155.

Yang, L., van Hinsberg, V. J. & Samson, I. M. (2018). A new method to deconvolute binary mixture in LA-ICP-MS analyses to quantify the composition of phases smaller than the laser spot size. *Journal of Analytical Atomic Spectrometry* **33**, 1518–1528.

Yao, L., Sun, C. & Liang, Y. (2012). A parameterized model for REE distribution between low-Ca pyroxene and basaltic melts with applications to REE partitioning in low-Ca pyroxene along a mantle adiabat and during pyroxenite-derived melt and peridotite interaction. *Contributions to Mineralogy and Petrology* **164**, 261–280.